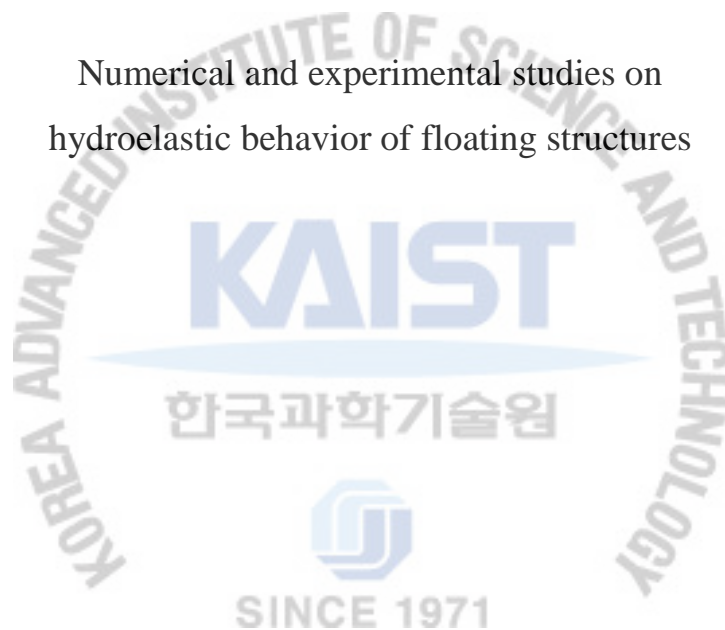


석사 학위논문  
Master's Thesis

부유식 구조물의 유탄성 거동에 관한  
수치적 및 실험적 연구

Numerical and experimental studies on  
hydroelastic behavior of floating structures



조 성 필 (趙 城 澤, Cho, Seong Pil)

기계항공시스템학부 해양시스템공학전공  
School of Mechanical, Aerospace and Systems Engineering  
Division of Ocean Systems Engineering

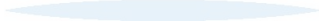
**KAIST**

2013

부유식 구조물의 유탄성 거동에 관한  
수치적 및 실험적 연구

Numerical and experimental studies on  
hydroelastic behavior of floating structures

KAIST

The logo for KAIST (Korea Advanced Institute of Science and Technology) is centered at the bottom of the page. It consists of the letters 'KAIST' in a bold, blue, sans-serif font. Below the text is a light blue, horizontal, oval-shaped shadow or underline.

# Numerical and experimental studies on hydroelastic behavior of floating structures

Advisor : Professor Lee, Phill-Seung

Co-advisor : Professor Cho, Yeun-Woo

by

Cho, Seong-Pil

School of Mechanical, Aerospace and Systems Engineering  
Division of Ocean Systems Engineering

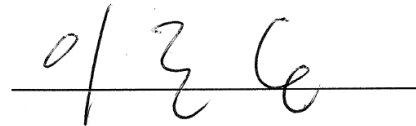
KAIST

A thesis submitted to the faculty of KAIST in partial fulfillment of the requirements for the degree of Master of Science and Engineering in the School of Mechanical, Aerospace and Systems Engineering, Division of Ocean Systems Engineering. The study was conducted in accordance with Code of Research Ethics<sup>1</sup>

2012. 12. 21

Approved by

Associate Professor Lee, Phill-Seung



---

<sup>1</sup> Declaration of Ethical Conduct in Research: I, as a graduate student of KAIST, hereby declare that I have not committed any acts that may damage the credibility of my research. These include, but are not limited to: falsification, thesis written by someone else, distortion of research findings or plagiarism. I affirm that my thesis contains honest conclusions based on my own careful research under the guidance of my thesis advisor.

부유식 구조물의 유탄성 거동에 관한  
수치적 및 실험적 연구

조 성 필

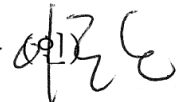
위 논문은 한국과학기술원 석사학위논문으로  
학위논문심사위원회에서 심사 통과하였음.

KAIST

2012 년 12 월 21 일

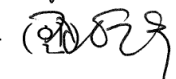
심사위원장

이 필 승



심사위원

조 연 우



심사위원

김 병 완



MOSE  
20113598

조 성 필. Cho, Seong-Pil. Numerical and experimental studies on hydroelastic behavior of floating structures. 부유식 구조물의 유탄성 거동에 관한 수치적 및 실험적 연구. Division of Ocean Systems Engineering. 2013. 54 p. Advisor Prof. Lee, Phill-Seung. Text in English

### ABSTRACT

The purpose of this study is to evaluate numerical solutions for the hydroelastic behavior of floating structures with hinge connections under regular waves based on the frequency domain. In order to model the floating structure, we employed a MITC plate element using a mixed formulation, and the fluid-structure interface boundary surface is also discretized to solve coupled equations. Two conditions, a stiffness parameter and characteristic length, are needed to evaluate the region of hydroelasticity. The experimental study is based on measurement of the hydroelastic behavior on a mat-like structure. The measurement is focused on heave motion and bending moment. The results from the experiment are presented to evaluate numerical solutions related to hydroelastic behavior.

Keywords: very large floating structures, finite element method (FEM), boundary element method (BEM) hydroelastic analysis, hinge connection, heave motion, bending moment

# Table of Contents

<b>Abstract</b> .....	<b>i</b>
<b>Table of Contents</b> .....	<b>ii</b>
<b>List of Tables</b> .....	<b>iii</b>
<b>List of Figures</b> .....	<b>iv</b>
<b>Chapter 1. Introduction</b> .....	<b>01</b>
<b>Chapter 2. General theory</b> .....	<b>03</b>
2.1 Overall description and assumptions .....	03
2.2 Formulations of the floating structure .....	04
2.3 Formulations of the fluid .....	06
2.4 Dimensionless parameters .....	09
<b>Chapter 3. Numerical methods</b> .....	<b>10</b>
3.1 MITC4 plate element .....	10
3.2 Static condensation method .....	12
3.3 Boundary elements .....	13
3.4 Discretization of the coupled equations .....	14
3.5 Treatment of singularity .....	16
3.6 Bending moment calculation .....	17
<b>Chapter 4. Experiment</b> .....	<b>19</b>
4.1 Experimental environment .....	19
4.2 Experimental model .....	20
4.3 The conditions of hydroelasticity .....	23
4.4 Linear wave theory .....	25
4.5 Measuring methods .....	26
<b>Chapter 5. Result</b> .....	<b>29</b>
5.1 Heave motion .....	29
5.2 Bending moment .....	43
<b>Chapter 6. Conclusion</b> .....	<b>49</b>
<b>References</b> .....	<b>50</b>
<b>Summary</b> .....	<b>52</b>

## List of Tables

**Table 4.1: The experimental conditions**

**Table 4.2: Information of floating structure model**

**Table 4.3: Experimental results of bending stiffness  $EI$**

**Table 4.4: Values of stiffness parameter and characteristic length in structural model**

The logo for KAIST (Korea Advanced Institute of Science and Technology) is centered on the page. It consists of the letters "KAIST" in a bold, blue, sans-serif font. Below the text is a light blue, horizontal oval shape that tapers at both ends, serving as a base or shadow for the text.

## List of Figures

- Figure 1.1: Applications of Very Large Floating Structures (VLFS)
- Figure 2.1: Overall description of hydroelastic analysis for a floating structure
- Figure 2.2: Floating plate structure model
- Figure 2.3: Schema of the fluid domain
- Figure 3.1: The geometry of a plate element
- Figure 3.2: The geometry of a boundary element
- Figure 3.3: Bending stresses in plate element
- Figure 4.1: Ocean research basin
- Figure 4.2: Scheme of experimental setup
- Figure 4.3: Section of the model
- Figure 4.4: The position of hinge connection
- Figure 4.5: Bending test for measuring bending stiffness  $EI$  of a floating structure model
- Figure 4.6: Global response under a static load
- Figure 4.7: Mapping of global response of floating structures
- Figure 4.8: Ranges of validity of various wave theories as a function of  $H/h$  and  $h/\lambda$
- Figure 4.9: Vicon motion capture system
- Figure 4.10: The measuring position of heave motion
- Figure 4.11: Three elements strain rosette
- Figure 4.12: The measuring position of strain gauge
- Figure 5.1: Distribution of heave motion at  $\alpha = 0.6$
- Figure 5.2: Longitudinal distributions of heave motion (No hinge connection at  $\theta = 0^\circ$ )
- Figure 5.3: Longitudinal distributions of heave motion (No hinge connection at  $\theta = 30^\circ$ )
- Figure 5.4: Longitudinal distributions of heave motion (No hinge connection at  $\theta = 60^\circ$ )
- Figure 5.5: Longitudinal distributions of heave motion (No hinge connection at  $\theta = 90^\circ$ )
- Figure 5.6: Longitudinal distributions of heave motion (One hinge connection at  $\theta = 0^\circ$ )
- Figure 5.7: Longitudinal distributions of heave motion (One hinge connection at  $\theta = 30^\circ$ )
- Figure 5.8: Longitudinal distributions of heave motion (One hinge connection at  $\theta = 60^\circ$ )
- Figure 5.9: Longitudinal distributions of heave motion (One hinge connection at  $\theta = 90^\circ$ )
- Figure 5.10: Longitudinal distributions of heave motion (Two hinge connection at  $\theta = 0^\circ$ )

**Figure 5.11: Longitudinal distributions of heave motion (Two hinge connection at  $\theta = 30^\circ$ )**

**Figure 5.12: Longitudinal distributions of heave motion (Two hinge connection at  $\theta = 60^\circ$ )**

**Figure 5.13: Longitudinal distributions of heave motion (Two hinge connection at  $\theta = 90^\circ$ )**

**Figure 5.14: The position of neutral axis**

**Figure 5.15: Distribution of bending moment at  $\alpha = 0.6$**

**Figure 5.16: Longitudinal distributions of bending moment (One hinge connection at  $\theta = 0, 30^\circ$ )**

**Figure 5.17: Longitudinal distributions of bending moment (One hinge connection at  $\theta = 60, 90^\circ$ )**

**Figure 5.18: Longitudinal distributions of bending moment (Two hinge connection at  $\theta = 0, 30^\circ$ )**

**Figure 5.19: Longitudinal distributions of bending moment (Two hinge connection at  $\theta = 60, 90^\circ$ )**

The logo for KAIST (Korea Advanced Institute of Science and Technology) is centered on the page. It consists of the letters "KAIST" in a bold, blue, sans-serif font. Below the text is a light blue, horizontal, oval-shaped shadow or underline.

# Chapter 1. Introduction

Very large floating structures (VLFS) demand new technology for the analysis of their structural behavior due to severe ocean environments. A VLFS is a structure that has elastic behavior with the external environment, such as waves, currents, and wind load due to a lack of bending stiffness. This phenomenon is widely known as hydroelasticity. For many hydroelastic behaviors of a floating structure, heave motion (the vertical displacement) and bending moment are the most important quantities. In recent years, VLFS are being developed as floating oil storage containers, airports, and bridges, as illustrated in Figure 1.1.

Since VLFS are huge structures applied in the real world, it is very difficult to construct them as a single structure on the ground. Therefore, VLFS are constructed by many combined units that make up the structure in the sea. In order to construct VLFS in the sea, the connection type for each unit of the floating structure should be considered. The hinge connection is the best option to reduce the bending moment acting on the cross section of the structure. Accordingly, many studies have been performed on the hydroelastic behavior of floating structures with connection types. B.W. Kim [5] investigated a floating structure with hinge and spring connections using a numerical analysis with the direct method. S. Fu [16] investigated the effect of the hinge connection by adjusting the rotational stiffness of the hinge using a prototype structure model. A floating beam model that was divided into auxiliary and main parts was used to investigate the optimum connection design for floating structures by M. Riyansyah [17].

While many studies have been carried out on VLFS with hinge connections using the numerical analysis approach, there has been little research to verify the hydroelastic behavior of floating structures with hinge connections. K. Yago [1] conducted an experimental study of the hydroelastic response of a floating structure with a large-scale model without hinge connections through a tank test. M. Riyansyah [17] experimentally evaluated the hydroelastic response of a floating structure with one hinge connection acting on a zero degree incident wave. This study is limited in its capacity to validate other numerical studies, however, because only one incident angle and a few wave frequencies were considered. In order to overcome this shortcoming, we performed appropriate experiments on the hydroelastic behavior of a floating structure with hinge connections to verify the results of a numerical method. Main idea is that floating structures have different hydroelastic behavior depending on the number of hinge connections.

In this study, we first review the mathematical formulation and the numerical procedures to solve the hydroelastic problems of floating structures. Next, we demonstrate the experimental conditions and the data analysis procedure. Finally, we present the experimental results, which are related with the heave motion and bending moment with measuring systems. The experimental results and calculations demonstrate the

effectiveness of the hinge connections in reducing the bending moment by proper measurement for the floating structure.



(a) Offshore airport



(b) Floating bridge



(c) Oil storage terminal

Figure 1.1: Applications of Very Large Floating Structures (VLFS)

## Chapter 2. General theory

In this chapter, we describe mathematical modeling and formulations of a hydroelastic analysis of floating structures. First, we present the physical assumptions, governing equations, and boundary conditions for the fluid and structure. Next, final equations are described in variational forms for the finite and boundary element methods in the frequency domain.

### 2.1 Overall description and assumptions

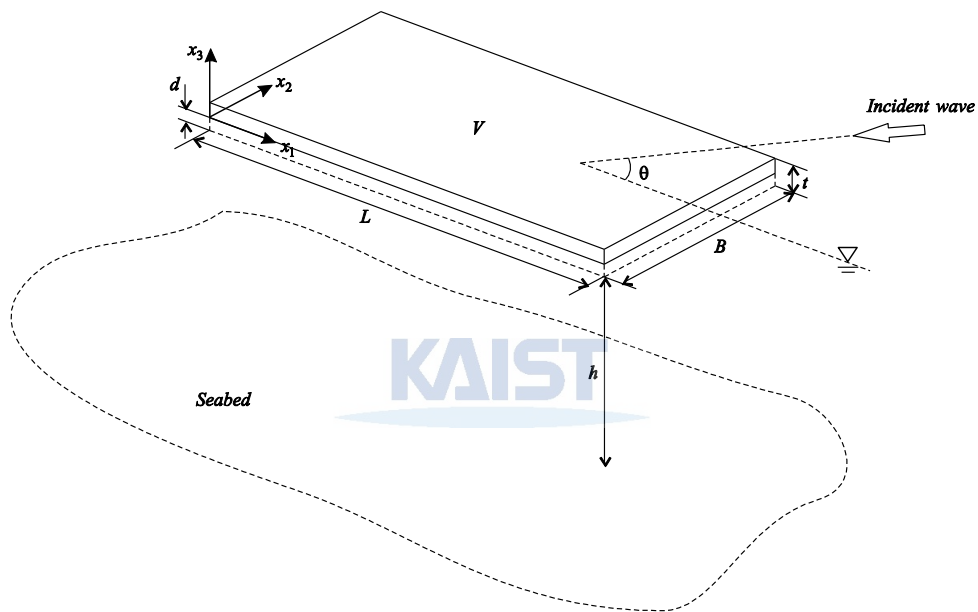


Figure 2.1: Overall description of hydroelastic analysis for a floating structure

Figure 2.1 provides an overall description of the hydroelastic analysis for a floating structure. The Very Large Floating Structure (VLFS) was modeled as a rectangular floating plate model (dimension  $L \times B \times t$ ). The draft and the water depth are denoted by  $d$  and  $h$ , respectively. The incident wave, which has small amplitude  $A$ , was induced to the floating plate with angular frequency  $\omega$  and angle  $\theta$ . Note that the draft  $d$  was calculated under the static equilibrium condition in the rigid body assumption.

In terms of material properties, the structure was assumed to be a homogeneous, isotropic, and linear elastic material with small displacement and strain. The fluid was assumed to be an ideal incompressible, inviscid fluid with irrotational flow. The external load was modeled by a regular wave that was moving toward the floating plate with a constant angular frequency.

## 2.2 Formulations of the floating structure

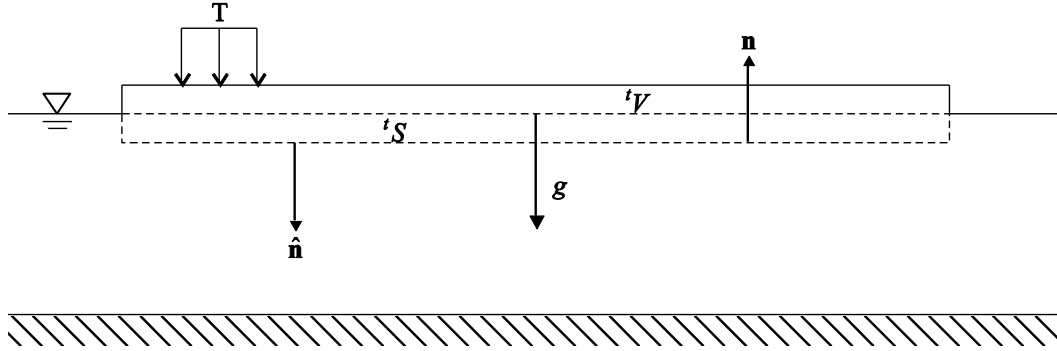


Figure 2.2: Floating plate structure model

In the static equilibrium condition,  ${}^tV$  and  ${}^tS$  are the current structure volume and wet surface of the floating structure, respectively. Then, the governing equations for body force and surface force are

$$\frac{\partial \sigma_{ij}}{\partial x_j} + \rho_s F_i - \rho_s U_i = 0 \quad \text{in } {}^tV \quad (2.1)$$

$$\sigma_{ij} \cdot n_j = T_i \quad \text{on } {}^tS \quad (2.2)$$

where  $\sigma_{ij}$  is the stress tensor and  $\rho_s$  is the structural density.  $F_i$ ,  $T_i$ , and  $U_i$  are the body force vector, surface force vector, and displacement vector, respectively.  $n_j$  denotes unit normal vectors extending outward from the structure domain.

After integration by parts and applying the divergence theorem, virtual work of the floating structure could be obtained by Eq. (2.3).  $\delta u_i$  and  $\delta \varepsilon_{ij}$  denote virtual displacement and virtual strain.

$$\int_{{}^tV} \rho_s \ddot{U}_i \delta u_i d{}^tV + \int_{{}^tV} \sigma_{ij} \delta \varepsilon_{ij} d{}^tV = \int_{{}^tV} \rho_s F_i \delta u_i d{}^tV + \int_{{}^tS} T_i \delta u_i d{}^tS \quad (2.3)$$

In matrix form,

$$\int_{{}^tV} \rho_s \delta \mathbf{u}^T \ddot{\mathbf{U}} d{}^tV + \int_{{}^tV} \delta \boldsymbol{\varepsilon}^T \boldsymbol{\sigma} d{}^tV = \int_{{}^tV} \rho_s \delta \mathbf{u}^T \mathbf{F} d{}^tV + \int_{{}^tS} T_i \delta u_i d{}^tS \quad (2.4)$$

In a static equilibrium state, the initial stress condition could be neglected as the initial acceleration is equal to zero. The applied body force is gravitational force in the vertical direction and surface force applied is pressure acting on the wet surface.

$$\mathbf{F} = \begin{bmatrix} 0 \\ 0 \\ -g \end{bmatrix}, \mathbf{T} = -P \begin{bmatrix} \hat{n}_1 \\ \hat{n}_2 \\ \hat{n}_3 \end{bmatrix} \quad (2.5)$$

By applying the initial stress condition and steady state problem to virtual work, the solution could be obtained by

$$\int_{t_V} \rho_s \delta \mathbf{u}^T \ddot{\mathbf{U}} d^t V + \int_{t_V} \delta \boldsymbol{\varepsilon}^T \boldsymbol{\sigma} d^t V = - \int_{t_S} P \delta \mathbf{u}^T \hat{\mathbf{n}} d^t S \quad (2.6)$$

Finally, we assumed

$$\mathbf{U} = u(x)e^{i\omega t}, \boldsymbol{\varepsilon} = \varepsilon(x)e^{i\omega t}, P = p(x)e^{i\omega t}, \hat{\mathbf{n}} = -\vec{\mathbf{n}} = \begin{bmatrix} 0 \\ 0 \\ -n_3 \end{bmatrix} \quad (2.7)$$

The final variational formulation of the structure for a steady state condition was obtained as

$$- \int_{t_V} \omega^2 \rho_s \delta u(x)^T u(x) d^t V + \int_{t_V} \delta \boldsymbol{\varepsilon}(x)^T \boldsymbol{\sigma}(x) d^t V = \int_{t_S} p(x) u_3 d^t S \quad (2.8)$$

In matrix form,

$$- \int_{t_V} \omega^2 \rho_s \delta \mathbf{u}^T \mathbf{u} d^t V + \int_{t_V} \delta \boldsymbol{\varepsilon}^T \boldsymbol{\sigma} d^t V = \int_{t_S} p(x) \mathbf{u}_3 d^t S \quad (2.9)$$

$p(x)$  is unknown pressure and  $u_3$  is displacement of  $x_3$  axis.

### 2.3 Formulations of the fluid

Since the fluid was assumed to be an ideal fluid that is invicid, incompressible, and irrotational, motions of fluid particles could be described by the velocity potential, which satisfies Laplace's equation and the boundary conditions. Eq. (2.10) is Laplace's equation for an ideal fluid in a steady state condition.

$$\nabla^2\Phi = 0, \Phi = \phi e^{i\omega t} \text{ in fluid domain.} \quad (2.10)$$

From the linear momentum conversation with the above assumptions and additional assumptions of a Newtonian, isotropic fluid, we can derive Bernoulli's equation for the potential fluid:

$$\frac{\partial\Phi}{\partial t} + \frac{1}{2}\nabla\Phi \cdot \nabla\Phi + \frac{\mathbf{P}}{\rho_w} + gu_3 = 0 \quad (2.11)$$

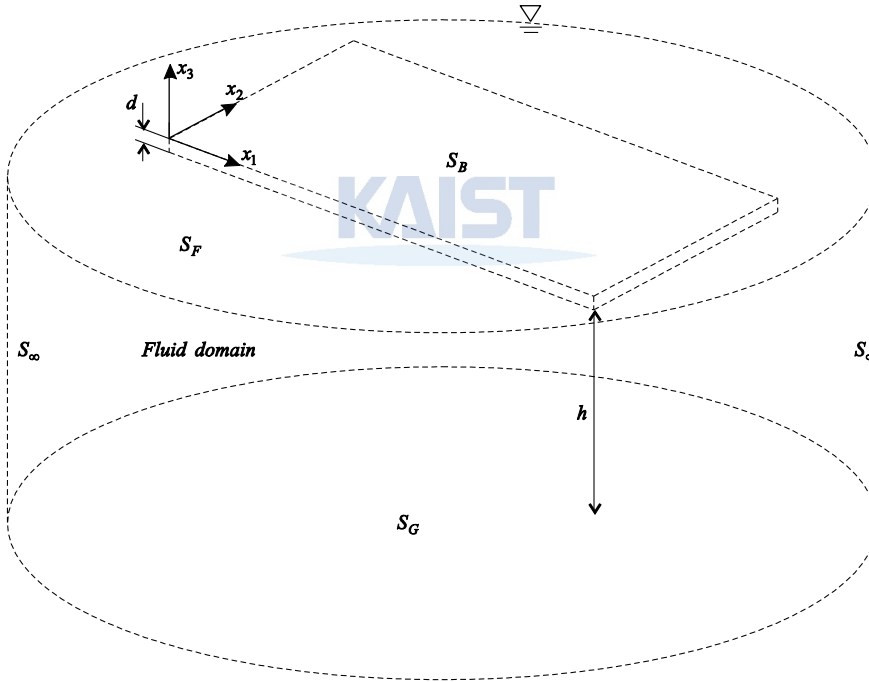


Figure 2.3: Schema of the fluid domain

As illustrated in Figure 2.3, fluid domain is defined by its surfaces:  $S_B$  (interface between the structure and the fluid);  $S_F$  (free surface);  $S_G$  (ground surface); and  $S_\infty$  (surface that envelops fluid domain).

Eqs. (2.12) to (2.15) describe the boundary conditions. The normal velocity of the structure and the fluid are the same on the interface surface, and the body boundary condition on the body surface is then,

$$\frac{\partial\phi}{\partial x_3} = i\omega u_3 \text{ on } S_B \quad (2.12)$$

We should consider two conditions: the kinematic boundary condition and the dynamic boundary condition. The free surface boundary condition is then obtained as

$$\frac{\partial \phi}{\partial x_3} = \frac{\omega^2}{g} \phi \quad \text{on } S_F \quad (2.13)$$

Given that the bottom does not move, we applied the kinematic condition.

$$\frac{\partial \phi}{\partial x_3} = 0 \quad \text{on } S_G \quad (2.14)$$

The radiated energy that the diffraction wave and the wave cause by the movements of the structure will move to infinity. This condition is called the Sommerfeld radiation condition:

$$\lim_{R \rightarrow \infty} \sqrt{R} \left( \frac{\partial}{\partial R} + ik \right) (\phi - \phi_I) = 0, \quad R = |x - \xi| \quad \text{on } S_\infty \quad (2.15)$$

$g$  is the gravitational acceleration and  $k$  is the wave number, respectively.  $R$  is the distance of the spatial point  $x$  and source point  $\xi$ . Because the floating structure was a thin structure compared with the water depth, we assumed the source point and spatial point are identically located in a free surface.

Eq. (2.16) is the incident potential  $\phi_I$  for a finite depth.

$$\phi_I = i \frac{gA}{\omega} \frac{\cosh k(x_3 + h)}{\cosh kh} e^{ik(x_1 \cos \theta + x_2 \sin \theta)} \quad \text{for the finite depth} \quad (2.16)$$

The above equations in the fluid domain were formulated as a boundary integral equation using the Green's function. Kim [7] conducted derivation of the relate formulations. The boundary integral equation on the body surface of the floating plate is

$$-4\pi\phi(x) + 4\pi\phi_I(x) = \int_{S_B} \left( \phi(\xi) \frac{\omega^2}{g} G(x; \xi) - G(x; \xi) i\omega u_3 \right) dS_B(\xi) \quad (2.17)$$

Eq. (2.17) is the boundary integral equation on the body surface of the floating structure and  $G(x; \xi)$  is a free surface Green's function for water of finite depth that satisfies the boundary conditions. In infinite and finite depths with the source potential, the Green's function was defined by Wehausen and Laitone [19]. In order to overcome the complexities of integration of the Green's function, an efficient algorithm developed by Newmann [20] was adopted. Therefore, the final variational formulation of the fluid for the steady state condition was obtained as Eq. (2.18).

$$\int_{S_B} \delta P(x)^T u_3(x) dS_B(x) + \frac{1}{g\rho_w} \int_{S_B} \delta P(x)^T P(x) dS_B(x) + \frac{1}{4\pi g^2 \rho_w} \int_{S_B} \delta P(x)^T \left( \int_{S_B} P(\xi) G(x; \xi) dS_B(\xi) \right) dS_B(x) = -i \frac{\omega}{g} \int_{S_B} \delta P(x)^T \phi_I(x) dS_B(x) \quad (2.18)$$

$\rho_w$  is the fluid density. The actual volume and surface of the structure occupied at time  $t$  change periodically from the static equilibrium state; however, because of the assumption of small displacements, the variations of the volume and surface are negligible.

The logo for KAIST (Korea Advanced Institute of Science and Technology) is centered on the page. It consists of the letters "KAIST" in a bold, blue, sans-serif font. Below the text is a light blue, horizontal, oval-shaped shadow or underline.

## 2.4 Dimensionless parameters

In the definition of problems, dimensionless parameters are usually used for generalization of parameters. In this paper, we suggested three parameters: stiffness parameter  $S$ , aspect ratio length / breadth ( $L / B$ ), and the dimensionless wave length  $\alpha$ . The significance of hydroelasticity is related to a stiffness parameter  $S$  proposed by Newmman [11], which corresponds physically to the ratio between the internal force due to bending of the modules and the corresponding hydrostatic restoring force. Newmman concluded that the important regime for significant hydroelastic effects is  $10^{-6} \leq S \leq 10^{-2}$ . The parameters about the structure and fluid contain specific information about the bending stiffness and geometry and incident wave travelling towards the structure, in  $S$ , the aspect ratio, and  $\alpha$ , respectively. Eq. (2.19) describes the physical meaning of the equation.

$$S = \frac{EI}{\rho_w g L^5}, \quad \text{Aspect ratio} = \frac{L}{B}, \quad \alpha = \frac{\lambda}{L} \quad (2.19)$$

$EI$  is the bending stiffness of the structure,  $k_c$  the spring constant of hydroelastic restoring force, and  $\lambda$  is the wave length.

The logo for KAIST (Korea Advanced Institute of Science and Technology) is displayed in a light blue, semi-transparent font. It consists of the letters 'KAIST' in a bold, sans-serif typeface, with a horizontal line underneath the letters.

## Chapter 3. Numerical methods

In this chapter, we describe methods for solving the equations of the fluid and structure parts into plate structures. With the plate structure in the structural and fluid domains, we applied the finite element method (FEM) and boundary element method, respectively. The static condensation method was employed in modeling the hinge connection in the structural domain. Finally, the coupled equation was transformed to a matrix form with relation to structural displacement and fluid pressure.

### 3.1 MITC4 plate element

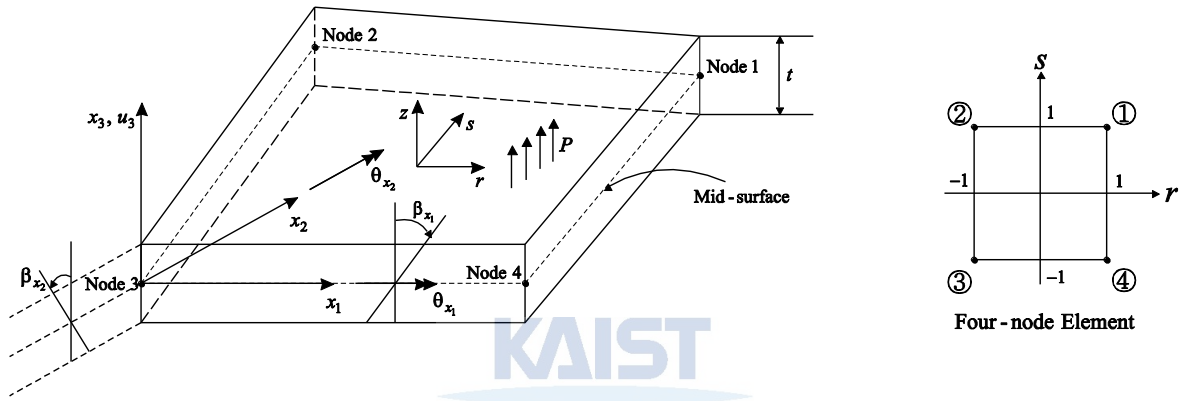


Figure 3.1: The geometry of a plate element

The plate formulation is a special case of the general shell element formulation and is based on the theory of plates with transverse shear deformations. This theory, developed by E. Reissner [24] and R.D. Mindlin [25], uses the assumption that particles of the plate originally on a straight line that is normal to the un-deformed middle surface remain on a straight line during deformation, but this line is not necessarily normal to the deformed middle surface. With this assumption, the displacement components of point coordinates  $x_1$ ,  $x_2$ , and  $x_3$  are,

$$\mathbf{u} = \begin{bmatrix} u_1 \\ u_2 \\ u_3 \end{bmatrix} = \begin{bmatrix} -x_3 \beta_{x_1}(x, y) \\ -x_3 \beta_{x_2}(x, y) \\ u_3(x, y) \end{bmatrix} = \begin{bmatrix} x_3 \sum_{i=1}^4 h_i \theta_{x_2}^i \\ -x_3 \sum_{i=1}^4 h_i \theta_{x_1}^i \\ \sum_{i=1}^4 h_i u_{3i} \end{bmatrix} \quad (3.1)$$

$u_3$  is the transverse displacement,  $\beta_{x_1}$  and  $\beta_{x_2}$  are the rotations normal to the undeformed middle surface in  $x_1, x_3$  and  $x_2, x_3$ . In the pure displacement discretization,  $\beta_{x_1}$  and  $\beta_{x_2}$  are transformed into  $\theta_{x_2}$ ,  $\theta_{x_1}$ . The bending strains vary linearly through the plate thickness and are given by the curvatures of the plate.

With the assumption that stress in the direction of thickness is zero, for an isotropic material, the state of bending strain and stress are

$$\begin{bmatrix} \varepsilon_{11} \\ \varepsilon_{22} \\ \gamma_{12} \end{bmatrix} = -x_3 \begin{bmatrix} \frac{\partial \beta_{x_1}}{\partial x_1} \\ \frac{\partial \beta_{x_2}}{\partial x_2} \\ \frac{\partial \beta_{x_1}}{\partial x_2} + \frac{\partial \beta_{x_2}}{\partial x_1} \end{bmatrix}, \quad \begin{bmatrix} \sigma_{11} \\ \sigma_{22} \\ \sigma_{12} \end{bmatrix} = -x_3 \frac{E}{(1-\nu^2)} \begin{bmatrix} 1 & \nu & 0 \\ \nu & 1 & 0 \\ 0 & 0 & \frac{1-\nu}{2} \end{bmatrix} \begin{bmatrix} \frac{\partial \beta_{x_1}}{\partial x_1} \\ \frac{\partial \beta_{x_2}}{\partial x_2} \\ \frac{\partial \beta_{x_1}}{\partial x_2} + \frac{\partial \beta_{x_2}}{\partial x_1} \end{bmatrix} \quad (3.2)$$

MITC4 elements proposed by Bathe, K.J. [1] are utilized in the plate formulation. A contravariant base vector was used in the formulation and its relation with a covariant base vector is explained through a Kronecker delta function.

$$\mathbf{g}_i \cdot \mathbf{g}^j = \delta_i^j \begin{cases} 0, i \neq j \\ 1, i = j \end{cases}, \quad \mathbf{g}_i \cdot = \frac{\partial^0 \mathbf{x}}{\partial r_i} \quad (3.3)$$

The essence of the MITC4 formulation lies in the separate interpolation of the transverse displacement (section rotation) and of the transverse shear strains. As described earlier, the displacement and rotations are interpolated as usual, but for the transverse shear strains, the covariant components measured in the natural coordinate system are interpolated. The transverse shear strains will be as follows

$$\boldsymbol{\gamma} = \begin{bmatrix} \gamma_{13} \\ \gamma_{23} \end{bmatrix} = \begin{bmatrix} 2\tilde{\boldsymbol{\varepsilon}}_{rx_3}(\mathbf{g}^r \cdot \mathbf{e}_{x_1})(\mathbf{g}^{x_3} \cdot \mathbf{e}_{x_3}) + 2\tilde{\boldsymbol{\varepsilon}}_{sz}(\mathbf{g}^s \cdot \mathbf{e}_{x_1})(\mathbf{g}^{x_3} \cdot \mathbf{e}_{x_3}) \\ 2\tilde{\boldsymbol{\varepsilon}}_{rx_3}(\mathbf{g}^r \cdot \mathbf{e}_{x_2})(\mathbf{g}^{x_3} \cdot \mathbf{e}_{x_3}) + 2\tilde{\boldsymbol{\varepsilon}}_{sz}(\mathbf{g}^s \cdot \mathbf{e}_{x_2})(\mathbf{g}^{x_3} \cdot \mathbf{e}_{x_3}) \end{bmatrix} \quad (3.4)$$

$$\begin{aligned} \tilde{\boldsymbol{\varepsilon}}_{rx_3} &= \frac{1}{2}(1+s)\tilde{\boldsymbol{\varepsilon}}_{rx_3}^A + \frac{1}{2}(1-s)\tilde{\boldsymbol{\varepsilon}}_{rx_3}^C = \frac{1}{8}(1+s) \left[ \frac{h}{2}(x_{3_1} - x_{3_2}) - \frac{h}{4}(x_{2_1} - x_{2_2})(\theta_{x_1}^1 - \theta_{x_1}^2) + \frac{h}{4}(x_{1_1} - x_{1_2})(\theta_{x_2}^1 - \theta_{x_2}^2) \right] \\ &\quad + \frac{1}{8}(1-s) \left[ \frac{h}{2}(x_{3_4} - x_{3_3}) - \frac{h}{4}(x_{2_4} - x_{2_3})(\theta_{x_1}^4 - \theta_{x_1}^3) + \frac{h}{4}(x_{1_4} - x_{1_3})(\theta_{x_2}^4 - \theta_{x_2}^3) \right] \end{aligned}$$

$$\begin{aligned} \tilde{\boldsymbol{\varepsilon}}_{sx_3} &= \frac{1}{2}(1+r)\tilde{\boldsymbol{\varepsilon}}_{sx_3}^D + \frac{1}{2}(1-r)\tilde{\boldsymbol{\varepsilon}}_{sx_3}^B = \frac{1}{8}(1+r) \left[ \frac{h}{2}(x_{3_1} - x_{3_4}) - \frac{h}{4}(x_{2_1} - x_{2_4})(\theta_{x_1}^1 - \theta_{x_1}^4) + \frac{h}{4}(x_{1_1} - x_{1_4})(\theta_{x_2}^1 - \theta_{x_2}^4) \right] \\ &\quad + \frac{1}{8}(1-r) \left[ \frac{h}{2}(x_{3_2} - x_{3_3}) - \frac{h}{4}(x_{2_2} - x_{2_3})(\theta_{x_1}^2 - \theta_{x_1}^3) + \frac{h}{4}(x_{1_2} - x_{1_3})(\theta_{x_2}^2 - \theta_{x_2}^3) \right] \end{aligned}$$

$$\mathbf{g}^r = \sqrt{g^{rr}}(\sin \beta \mathbf{e}_{x_1} - \cos \beta \mathbf{e}_{x_2}), \quad \mathbf{g}^s = \sqrt{g^{ss}}(\sin \alpha \mathbf{e}_{x_1} - \cos \alpha \mathbf{e}_{x_2}), \quad \mathbf{g}^{x_3} = \sqrt{g^{x_3 x_3}} \mathbf{e}_{x_3} \quad (3.5)$$

### 3.2 Static condensation method

In the finite element of the plate structure, the static condensation method (Ref. [16]) was applied to model the hinge connection. Static condensation is employed to reduce the number of the element's degrees of freedom and thus, in effect, to perform part of the solution of the total finite element system equilibrium equations prior to assembling the structure matrices of the structural stiffness  $\mathbf{K}$  and force vectors  $\mathbf{R}$ . In the plate element, rotation in the x or y direction will be condensed out, depending on the location and axis of the hinge connection. The condensed elements connected in a row in the floating structure could rotate to the longitudinal or breadth direction.

In order to establish equations used in the static condensation, it was assumed that the stiffness matrix and corresponding displacement and force vectors of the element under consideration are partitioned into the form,

$$\begin{bmatrix} \mathbf{K}_{aa} & \mathbf{K}_{ac} \\ \mathbf{K}_{ca} & \mathbf{K}_{cc} \end{bmatrix} \begin{bmatrix} \mathbf{U}_a \\ \mathbf{U}_c \end{bmatrix} = \begin{bmatrix} \mathbf{R}_a \\ \mathbf{R}_c \end{bmatrix} \quad (3.6)$$

where  $\mathbf{U}_a$  is the vector displacement to be retained and  $\mathbf{U}_c$  is the vector displacement to be condensed out, respectively. Using the second equation in the matrix, we can obtain,

$$\mathbf{U}_c = \mathbf{K}_{cc}^{-1}(\mathbf{R}_c - \mathbf{K}_{ca}\mathbf{U}_a) \quad (3.7)$$

This relation is used in the first equation to substitute  $\mathbf{U}_c$ , and then the condensed equation can be obtained and  $\mathbf{U}_c$  will disappear from the stiffness matrix. Later, the information of  $\mathbf{K}_{cc}^{-1}$  and  $\mathbf{K}_{ca}$  for each element through condensation will be used for re-condensation for calculation of bending moments.

$$(\mathbf{K}_{aa} - \mathbf{K}_{ac}\mathbf{K}_{cc}^{-1}\mathbf{K}_{ca})\mathbf{U}_a = \mathbf{R}_a - \mathbf{K}_{ac}\mathbf{K}_{cc}^{-1}\mathbf{R}_c \quad (3.8)$$

Using the static condensation method explained before, the implementation in the plate structure will start from rearrangement of the stiffness matrix according to the form of the condensation matrix. The process then follows the condensation process. The process is finished by re-assembly of the stiffness matrix. For the plate problem, for each element, static condensation is performed twice, because two nodes at the side of element are needed to define the hinge connection.

The advantage of using static condensation on the element level is that the order of the system matrices is reduced, which may mean that use of back-up storage is prevented. In addition, if subsequent elements are identical, the stiffness matrix of only the first element needs to be derived, and performing static condensation on the element internal degrees of freedom also reduces the computational effort required.

### 3.3 Boundary elements

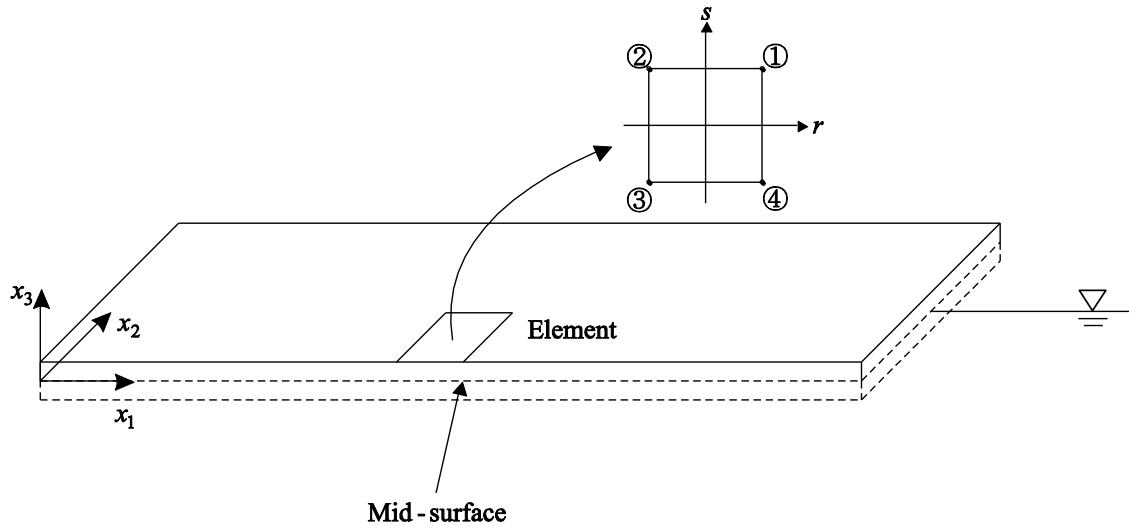


Figure 3.2: The geometry of a boundary element

The boundary elements method (BEM) was applied for the fluid by dividing the wet surface interface of the fluid with the structure into elements of four nodes. The boundary surface is the mid-surface of the plate structure in the equilibrium state because the plate thickness is very small, compared to its length and width. This method was applied in the coupled equations. Then, the interpolated pressure on the middle surface for four nodes boundary elements is

$$P(r, s) = \sum_{k=1}^4 h_k P \tag{3.9}$$

### 3.4 Discretization of the coupled equations

The coupled equations were transformed to matrices form to apply MITC4 plate elements and boundary elements. The structural volume was divided into N elements and body boundary surface into M elements. MITC4 plate elements are then applied to Eq.(2.9) as follows:

$$\begin{aligned}
 & -\omega^2 \rho_s t \sum_{e=1}^N \left[ {}_e \hat{\mathbf{u}}^T \int_{-1}^1 \int_{-1}^1 \mathbf{H}_u^T \mathbf{H}_u \det(\mathbf{J}) dr ds {}_e \hat{\mathbf{u}} \right] - \sum_{e=1}^M \left[ {}_e \hat{\mathbf{u}}^T \int_{-1}^1 \int_{-1}^1 \mathbf{h}_{u_3}^T \mathbf{h}_p \det(\mathbf{J}) dr ds {}_e \hat{\mathbf{P}} \right] \\
 & + \sum_{e=1}^N \left[ {}_e \hat{\mathbf{u}}^T \left( \int_{-1}^1 \int_{-1}^1 \mathbf{B}_\kappa^T \mathbf{C}_b \mathbf{B}_\kappa \det(\mathbf{J}) dr ds + \int_{-1}^1 \int_{-1}^1 \mathbf{B}_\gamma^T \mathbf{C}_s \mathbf{B}_\gamma \det(\mathbf{J}) dr ds \right) {}_e \hat{\mathbf{u}} \right] = 0
 \end{aligned} \tag{3.10}$$

Boundary elements are applied to Eq.(2.19) as follows:

$$\begin{aligned}
 & \sum_{e=1}^M \left[ {}_e \hat{\mathbf{P}}^T \int_{-1}^1 \int_{-1}^1 \mathbf{h}_p^T \mathbf{h}_{u_3} \det(\mathbf{J}) dr ds {}_e \hat{\mathbf{u}} \right] + \sum_{e=1}^M \left[ {}_e \hat{\mathbf{P}}^T \frac{1}{g \rho_w} \int_{-1}^1 \int_{-1}^1 \mathbf{h}_p^T \mathbf{h}_p \det(\mathbf{J}) dr ds {}_e \hat{\mathbf{P}} \right] \\
 & + \sum_{e=1}^M \sum_{e'=1}^M \left[ {}_e \hat{\mathbf{P}}^T \frac{\omega^2}{4\pi g^2 \rho_w} \int_{-1}^1 \int_{-1}^1 \mathbf{h}_p^T \left( \int_{-1}^1 \int_{-1}^1 G(r, s; r', s') \mathbf{h}_p \det(\mathbf{J}) dr' ds' \right) \det(\mathbf{J}) dr ds {}_e \hat{\mathbf{P}} \right] \\
 & + \sum_{e=1}^M \left[ {}_e \hat{\mathbf{P}}^T i \frac{\omega}{g} \int_{-1}^1 \int_{-1}^1 \mathbf{h}_p^T \phi_I \det(\mathbf{J}) dr ds \right] = 0
 \end{aligned} \tag{3.11}$$

$$\mathbf{h}_p = [h_1 \quad h_2 \quad h_3 \quad h_4]$$

$$\mathbf{h}_{u_3} = [h_1 \quad h_2 \quad h_3 \quad h_4 \quad 0 \quad 0]$$

$${}_e \hat{\mathbf{u}}^T = [{}_e x_{3_1} \quad {}_e x_{3_2} \quad {}_e x_{3_3} \quad {}_e x_{3_4} \quad {}_e \theta_{x_1}^1 \quad {}_e \theta_{x_1}^2 \quad {}_e \theta_{x_1}^3 \quad {}_e \theta_{x_1}^4 \quad {}_e \theta_{x_2}^1 \quad {}_e \theta_{x_2}^2 \quad {}_e \theta_{x_2}^3 \quad {}_e \theta_{x_2}^4]$$

$${}_e \hat{\mathbf{P}} = [{}_e P_1 \quad {}_e P_2 \quad {}_e P_3 \quad {}_e P_4]$$

$${}_e \mathbf{u}(r, s) = \mathbf{H}_u {}_e \hat{\mathbf{u}}, \quad {}_e \mathbf{u}_3(r, s) = \mathbf{h}_{u_3} {}_e \hat{\mathbf{u}}, \quad {}_e \mathbf{P}(r, s) = \mathbf{h}_p {}_e \hat{\mathbf{P}}$$

$${}_e \boldsymbol{\kappa} = \mathbf{B}_\kappa {}_e \hat{\mathbf{u}}, \quad {}_e \boldsymbol{\gamma} = \mathbf{B}_\gamma {}_e \hat{\mathbf{u}}$$

$$\mathbf{H}_u = \begin{bmatrix} 0 & 0 & 0 & 0 & 0 & 0 & 0 & 0 & x_3 h_1 & x_3 h_2 & x_3 h_3 & x_3 h_4 \\ 0 & 0 & 0 & 0 & -x_3 h_1 & -x_3 h_2 & -x_3 h_3 & -z h_4 & 0 & 0 & 0 & 0 \\ h_1 & h_2 & h_3 & h_4 & 0 & 0 & 0 & 0 & 0 & 0 & 0 & 0 \end{bmatrix}$$

$$\mathbf{C}_b = \frac{Et^3}{12} \begin{bmatrix} 1 & \nu & 0 \\ \nu & 1 & 0 \\ 0 & 0 & \frac{1-\nu}{2} \end{bmatrix}, \quad \boldsymbol{\kappa} = \begin{bmatrix} \frac{\partial \beta_{x_1}}{\partial x_1} \\ \frac{\partial \beta_{x_2}}{\partial x_2} \\ \frac{\partial \beta_{x_1}}{\partial x_2} + \frac{\partial \beta_{x_2}}{\partial x_1} \end{bmatrix}, \quad \mathbf{C}_s = \frac{Et \kappa}{2(1+\nu)} \begin{bmatrix} 1 & 0 \\ 0 & 1 \end{bmatrix} \tag{3.12}$$

The variational formulations, Eq. (3.10) and Eq. (3.11), were transformed into the final matrix forms by the finite and boundary elements discretization as

$$\begin{bmatrix} -\mathbf{S}_K + \mathbf{S}_M & \mathbf{S}_{\text{int}} \\ \mathbf{F}_{\text{int}} & \mathbf{F}_K + \mathbf{F}_M \end{bmatrix} \begin{bmatrix} \hat{\mathbf{u}} \\ \hat{\mathbf{P}} \end{bmatrix} = \begin{bmatrix} \mathbf{0} \\ \hat{\mathbf{F}}_I \end{bmatrix} \quad (3.13)$$

$\mathbf{S}_M$ ,  $\mathbf{S}_K$ , and  $\mathbf{S}_{\text{int}}$  are structural mass, stiffness, and interface matrices.  $\mathbf{F}_M$ ,  $\mathbf{F}_K$ , and  $\mathbf{F}_{\text{int}}$  are fluid mass, stiffness, and interface matrices.  $\hat{\mathbf{F}}_I$  is the external load vector due to the incident wave.  $\hat{\mathbf{u}}$  and  $\hat{\mathbf{P}}$  are the unknown displacement vector and pressure vector. If we divide the structural volume into  $N$  elements and the body surface into  $M$  elements,  $\hat{\mathbf{u}}$ ,  $\hat{\mathbf{P}}$ , and other matrices are defined by

$$\begin{aligned} \hat{\mathbf{u}}^T &= [u_3^1 \ \theta_{x_1}^1 \ \theta_{x_2}^1 \ u_3^2 \ \theta_{x_1}^2 \ \theta_{x_2}^2 \ \dots \ u_3^N \ \theta_{x_1}^N \ \theta_{x_2}^N], \quad \hat{\mathbf{P}}^T = [P_1 \ P_2 \ \dots \ P_M] \\ \delta \hat{\mathbf{u}}^T \mathbf{S}_M \hat{\mathbf{u}} &= \omega^2 \rho_s t \sum_{e=1}^N \left[ {}_e \delta \hat{\mathbf{u}}^T \int_{-1}^1 \int_{-1}^1 \mathbf{H}_u^T \mathbf{H}_u \det(\mathbf{J}) dr ds {}_e \hat{\mathbf{u}} \right] \\ \delta \hat{\mathbf{u}}^T \mathbf{S}_K \hat{\mathbf{u}} &= \sum_{e=1}^N \left[ {}_e \delta \hat{\mathbf{u}}^T \left( \int_{-1}^1 \int_{-1}^1 \mathbf{B}_\kappa^T \mathbf{C}_b \mathbf{B}_\kappa \det(\mathbf{J}) dr ds + \int_{-1}^1 \int_{-1}^1 \mathbf{B}_\gamma^T \mathbf{C}_s \mathbf{B}_\gamma \det(\mathbf{J}) dr ds \right) {}_e \hat{\mathbf{u}} \right] \\ \delta \hat{\mathbf{u}}^T \mathbf{S}_{\text{int}} \hat{\mathbf{P}} &= \sum_{e=1}^M \left[ {}_e \delta \hat{\mathbf{u}}^T \int_{-1}^1 \int_{-1}^1 \mathbf{h}_{u_3}^T \mathbf{h}_p \det(\mathbf{J}) dr ds {}_e \hat{\mathbf{P}} \right] \\ \delta \hat{\mathbf{P}}^T \mathbf{F}_{\text{int}} \hat{\mathbf{u}} &= \sum_{e=1}^M \left[ {}_e \delta \hat{\mathbf{P}}^T \int_{-1}^1 \int_{-1}^1 \mathbf{h}_p^T \mathbf{h}_{u_3} \det(\mathbf{J}) dr ds {}_e \hat{\mathbf{u}} \right] \\ \delta \hat{\mathbf{P}}^T \mathbf{F}_K \hat{\mathbf{P}} &+ \sum_{e=1}^M \left[ {}_e \delta \hat{\mathbf{P}}^T \frac{1}{g \rho_w} \int_{-1}^1 \int_{-1}^1 \mathbf{h}_p^T \mathbf{h}_p \det(\mathbf{J}) dr ds {}_e \hat{\mathbf{P}} \right] \\ \delta \hat{\mathbf{P}}^T \mathbf{F}_M \hat{\mathbf{P}} &= \sum_{e=1}^M \sum_{e'=1}^M \left[ {}_e \delta \hat{\mathbf{P}}^T \frac{\omega^2}{4\pi g^2 \rho_w} \int_{-1}^1 \int_{-1}^1 \mathbf{h}_p^T \left( \int_{-1}^1 \int_{-1}^1 G(r, s; r', s') \mathbf{h}_p \det(\mathbf{J}) dr' ds' \right) \det(\mathbf{J}) dr ds {}_e \hat{\mathbf{P}} \right] \\ \delta \hat{\mathbf{P}}^T \hat{\mathbf{F}}_I &= \sum_{e=1}^M \left[ {}_e \delta \hat{\mathbf{P}}^T i \frac{\omega}{g} \int_{-1}^1 \int_{-1}^1 \mathbf{h}_p^T \phi_I \det(\mathbf{J}) dr ds \right] \end{aligned} \quad (3.14)$$

### 3.5 Treatment of singularity

The Green function in the fluid equation has a singular value when the distance between the spatial point and the source point is close or equal to zero. The method to solve the singularity is focused on integration of the Green function. Singular components for the green function should be separated from its regular components. The integration of regular components of the Green function is solved by Gauss-Legendre quadrature. In order to understand this procedure; see Ref [7]. Kim [7] derived a method to deal with the singularities.

The logo for KAIST (Korea Advanced Institute of Science and Technology) is centered on the page. It consists of the letters "KAIST" in a bold, blue, sans-serif font. Below the text is a light blue, horizontal, oval-shaped shadow or underline.

### 3.6 Bending moment calculation

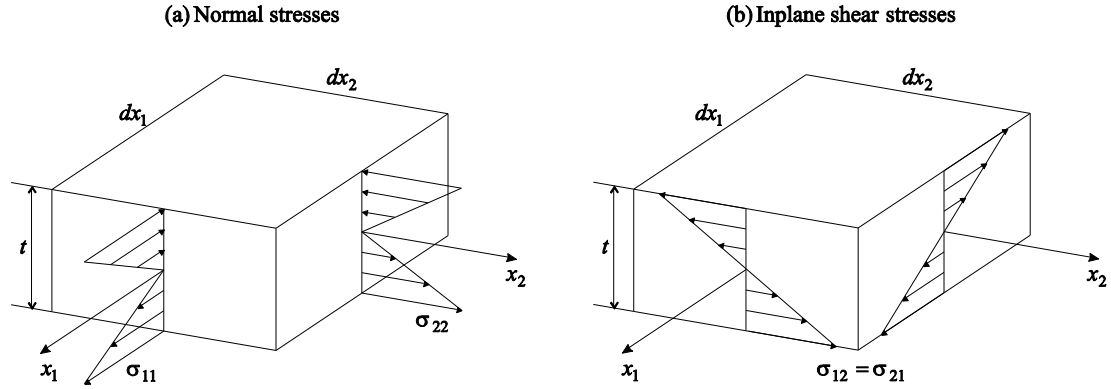


Figure 3.3: Bending stresses in plate element

The bending moments of  $M_{11}$ ,  $M_{22}$ , and  $M_{12}$  are stress resultants with dimensions of moment per unit length or force, that is, force. For example,  $Nm/m$ . The moments are calculated by integrating the elementary stress couples through the thickness:

$$\begin{aligned}
 M_{11} &= -\int_{-h/2}^{h/2} \sigma_{11} x_3 dx_3 = -\int_{-1}^1 \sigma_{11} \frac{t}{2} r_3 \det(\mathbf{J}) dr_3 \\
 M_{22} &= -\int_{-h/2}^{h/2} \sigma_{22} x_3 dx_3 = -\int_{-1}^1 \sigma_{22} \frac{t}{2} r_3 \det(\mathbf{J}) dr_3 \\
 M_{12} &= -\int_{-h/2}^{h/2} \sigma_{12} x_3 dx_3 = -\int_{-1}^1 \sigma_{12} \frac{t}{2} r_3 \det(\mathbf{J}) dr_3
 \end{aligned} \tag{3.15}$$

The integral relation between bending moments and stresses was solved by applying a numerical calculation. Displacement results of each element are used to obtain bending moments of each element in the plate structure. The overall result of node on the plate elements are the average value of bending moments at one node from four different elements.

$$\begin{aligned}
 \begin{bmatrix} M_{11} \\ M_{22} \\ M_{12} \end{bmatrix} &= \int_{-1}^1 \begin{bmatrix} \sigma_{11} \\ \sigma_{22} \\ \sigma_{12} \end{bmatrix} \frac{t}{2} r_3 \det(\mathbf{J}) dr_3 = \int_{-1}^1 x_3 \frac{E}{(1-\nu^2)} \begin{bmatrix} 1 & \nu & 0 \\ \nu & 1 & 0 \\ 0 & 0 & \frac{1-\nu}{2} \end{bmatrix} \begin{bmatrix} \frac{\partial \beta_{x_1}}{\partial x_1} \\ \frac{\partial \beta_{x_2}}{\partial x_2} \\ \frac{\partial \beta_{x_1}}{\partial x_2} + \frac{\partial \beta_{x_2}}{\partial x_1} \end{bmatrix} \frac{t}{2} r_3 \det(\mathbf{J}) dr_3 \\
 \begin{bmatrix} M_{11} \\ M_{22} \\ M_{12} \end{bmatrix} &= \int_{-1}^1 \frac{Et^3}{8(1-\nu^2)} r_3^2 \begin{bmatrix} 1 & \nu & 0 \\ \nu & 1 & 0 \\ 0 & 0 & \frac{1-\nu}{2} \end{bmatrix} \mathbf{B}_{\kappa \epsilon} \hat{\mathbf{u}} dr_3
 \end{aligned} \tag{3.16}$$

Another approach is an analytical method to calculate bending moments of the plate structure. This calculation method yields the integral equation of the previous bending moment equation. The results between the numerical and analytical methods showed no differences in bending moment values.

$$\begin{bmatrix} M_{11} \\ M_{22} \\ M_{12} \end{bmatrix} = \frac{Et^3}{12(1-\nu^2)} \begin{bmatrix} 1 & \nu & 0 \\ \nu & 1 & 0 \\ 0 & 0 & \frac{1-\nu}{2} \end{bmatrix} \mathbf{B}_{\kappa e} \hat{\mathbf{u}} \quad (3.17)$$

The logo for KAIST (Korea Advanced Institute of Science and Technology) is centered on the page. It consists of the letters "KAIST" in a bold, blue, sans-serif font. Below the text is a light blue, horizontal oval shape that tapers at both ends, resembling a stylized shadow or a base.

## Chapter 4. Experiment

### 4.1 Experimental environment

The experiment was carried out in the ocean research basin of the Division of Ocean Engineering at KAIST. Figure 4.1 shows the ocean research basin and Table 4.1 summarizes the experimental conditions. All experiments were conducted in calm water conditions. A plunge-type wave maker is an ideal tool for generating a linear regular wave. A beach-type wave absorber is a tool for efficiently absorbing the wave. However, for pursuing accurate data, we selected data that did not affect the reflection wave from the wave absorber. The floating structures were subjected to incident waves with four different incident wave angles (0, 30, 60, 90 deg.) and five different dimensionless wave lengths ( $\alpha$ , 0.1 ~ 1.0) in regular waves. Figure 4.2 illustrates the experimental setup in the ocean research basin.

Wave condition	Regular and linear wave
Incident wave angle	0, 30, 60, 90°
Incident wave amplitude (m)	0.005, 0.01
$\alpha$ ( $\lambda/L$ )	0.1 ~ 1.0
Water depth (m)	1.5

Table 4.1: The experimental conditions

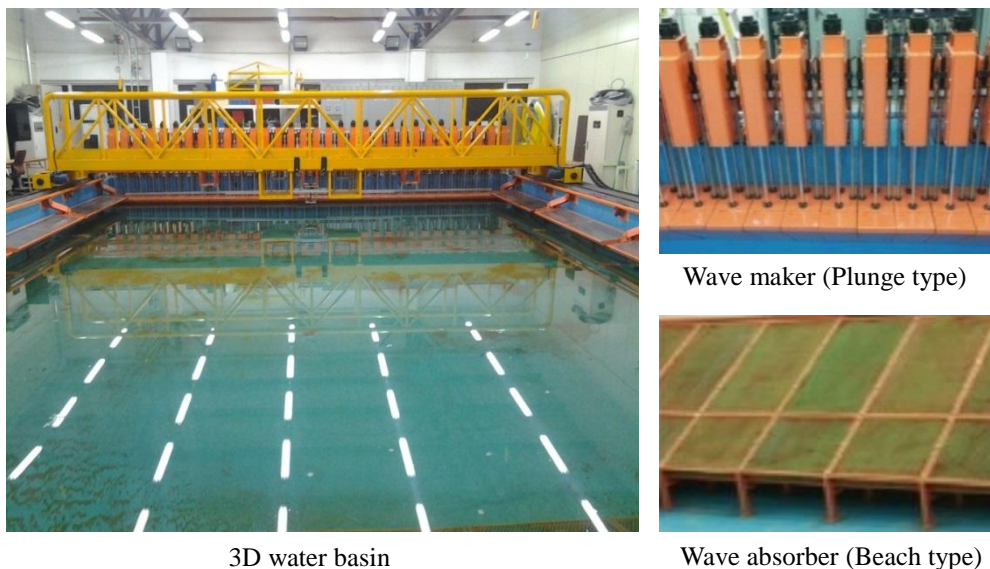


Figure 4.1: Ocean research basin

## 4.2 Experimental model

The experimental model for the floating structure is a mat-like structure of length 3m, breadth 0.6m, and thickness 0.04m. Table 4.2 lists the details of the floating structure model. In the floating structure, two materials were fabricated along the thickness direction, one of polycarbonate, and the other of polyethylene foam, which was used to buoy the structure. Figure 4.3 illustrates the structure of the composite plate. At four edge parts, the structure was moored by string at the basin surface upward. The string could remove the drift motion efficiently but was not expected to restrain heave motion. Therefore, this condition could assume a free state of the floating structure.

Length, $L$ (m)	3
Breadth, $B$ (m)	0.6
Thickness, $t$ (m)	0.04
Draft, $d$ (m)	0.011
Bending stiffness, $EI$ ( $Nm^2$ )	30.3845

Table 4.2: Information of floating structure model

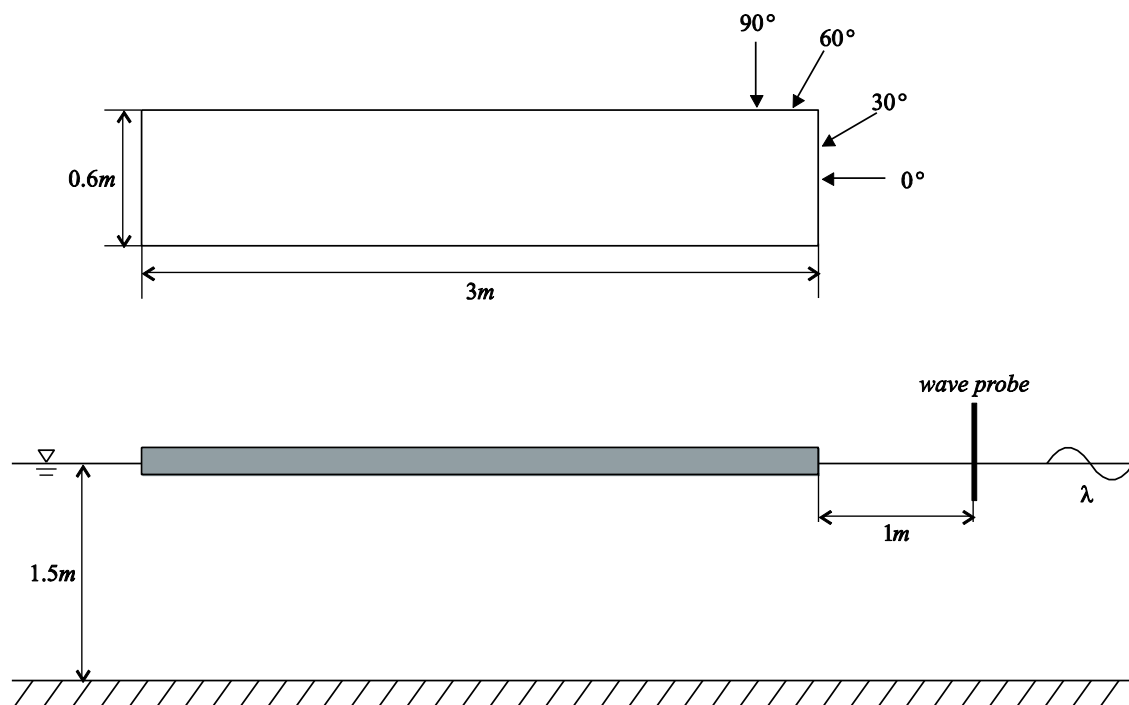


Figure 4.2: Scheme of experimental setup

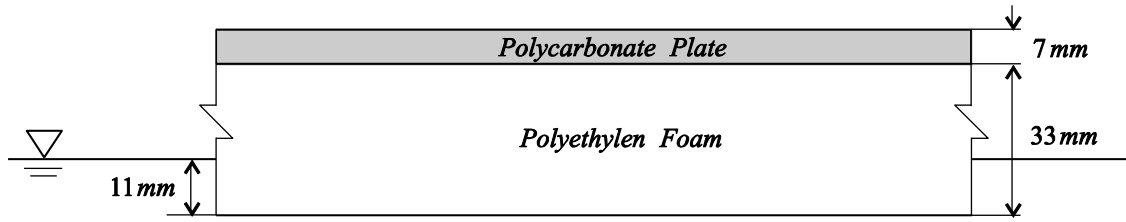


Figure 4.3: Section of the model

The hinge connection is a free rotation connection, which means that the rotational stiffness is equal to zero. The floating structure consists of hinge connections at one side of the structure. There were three cases: no hinge, one hinge connection, and two hinge connections. Figure 4.4 illustrates the position of the hinge connections.

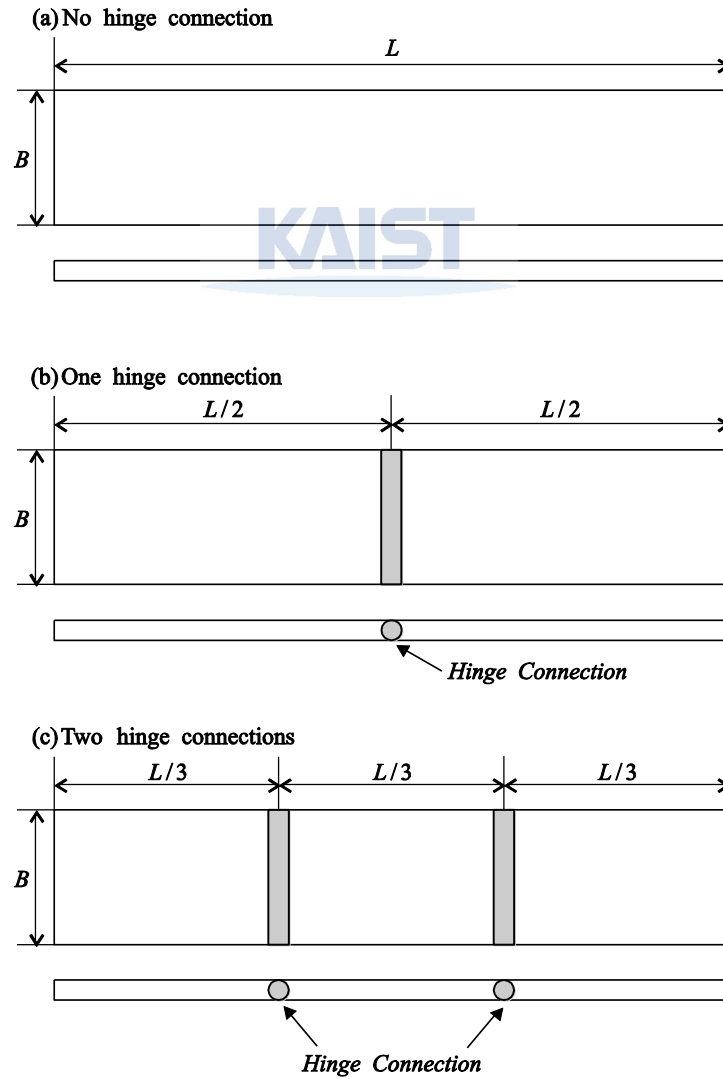


Figure 4.4: The position of hinge connection

In order to calculate the bending stiffness  $EI$ , a material test was conducted, as illustrated in Figure 4.5, which shows a cantilever beam under its own weight. This test was repeated four times with different lengths to check the repeatability of the calculated  $EI$ . The vertical deflection was measured at the free end of the cantilever to calculate  $EI$  from Eq. (4.1), which describes the deflection relation with the distributed load.

$$w = \frac{qL^4}{8EI} \quad (4.1)$$

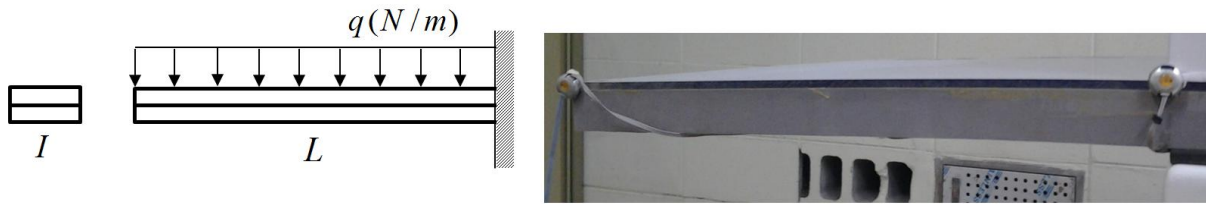


Figure 4.5: Bending test for measuring bending stiffness  $EI$  of a floating structure model

$w$  is the measured vertical deflection at the free end of the cantilever and  $q$  is the distributed load that was changed from its own weight. Table 4.3 summarizes the experimental results of four cases where the  $EI$  values converged to a single value.

KAIST

	Case 1	Case 2	Case 3	Case 4	Mean value
$L (m)$	0.375	0.5	0.6	0.7	
$w (m)$	0.00453	0.01464	0.0306	0.567	
$EI (Nm^2)$	31.019	30.335	30.095	30.089	30.3845

Table 4.3: Experimental results of bending stiffness  $EI$

### 4.3 The conditions of hydroelasticity

The structural model should be checked with respect to whether it is in a condition of hydroelastic behavior. Two conditions, the stiffness parameter  $S$  and characteristic length  $\lambda_c$ , are utilized to evaluate hydroelasticity. The stiffness parameter  $S$  is described in chapter 2.4.

As a rational measure to distinguish rigid body motion and hydroelastic behavior in terms of the global response of the floating structure, a characteristic length  $\lambda_c$  has been proposed by Suzuki [21].

$$\lambda_c = 2\pi \left( \frac{EI}{k_c} \right)^{\frac{1}{4}}, \quad k_c = \rho_w g B \quad (4.2)$$

$k_c$  is the spring constant of the hydrostatic restoring force.  $\lambda_c$  corresponds to the length of the locally deflected region by a static concentrated load, as illustrated in Figure 4.6. This indicates that the influence of an applied load on the elastic deformation is limited within the region of the length  $\lambda_c$ . The relationship between the wave length and the characteristic length is another important factor on the global response of floating structures. If the wave length is smaller than the characteristic length, the wave exciting forces alternate in the range of the length  $\lambda_c$  and the load effects cancel each other, resulting in a smaller global response. These characteristics of the global response with respect to the characteristic length are summarized in Figure 4.7.

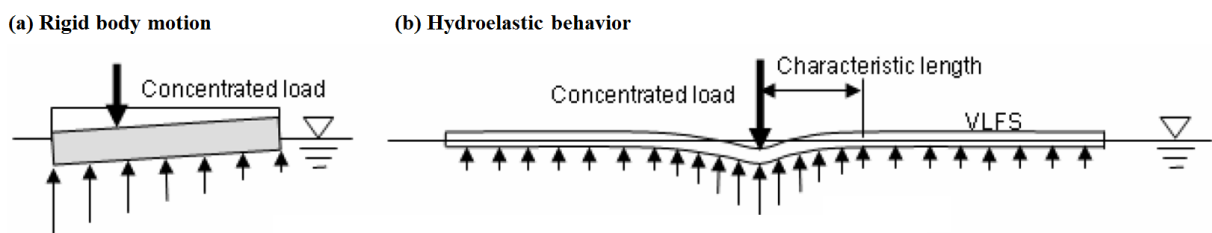


Figure 4.6: Global response under a static load

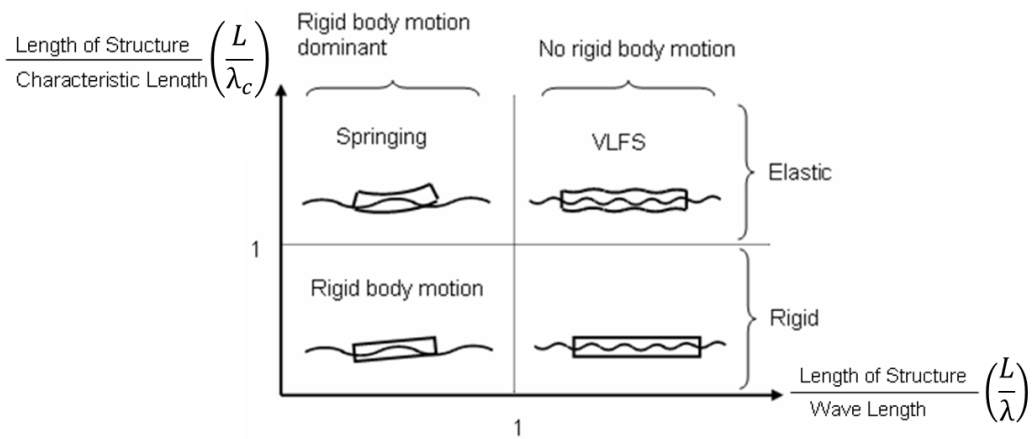


Figure 4.7: Mapping of global response of floating structures

In order to establish  $S$  and  $\lambda_c$  in accordance with the region of hydroelasticity,  $EI$  is the most important physical quantity. Table 4.5 demonstrate that both values satisfied the conditions of hydroelasticity.

Stiffness parameter ( $S$ )	Range	$10^{-6} \leq S \leq 10^{-2}$
	Model	$S = 1.2635 \times 10^{-5}$
Characteristic length ( $\lambda_c$ )	Range	$L > \lambda_c$
	Model	$\lambda_c = 1.6805$

Table 4.4: Values of stiffness parameter and characteristic length in structural model

#### 4.4 Linear wave theory

In one of the important assumptions, the incident wave should be a linear wave that satisfies linear wave theory in that the derived wave height is small compared with the water depth and wave length. In order to be applicable, the wave height, wavelength, and the water depth in linear wave theory have to meet certain condition. Komar [22] suggested the ranges of validity of various wave theories in terms of a function of wave steepness  $H/h$  and relative water depth  $h/\lambda$ . In the construction of this graph, the widest possible regions were given for simpler wave theories.

The relative water depth  $h/\lambda$  determined the water depth condition. Generally, if  $h/\lambda$  is more than 0.25, it designates a deep water condition and less than 0.05, a shallow water condition. Wave steepness related to wave height determines the wave property in various wave theories. From  $\alpha = 0.1$  to 1.0, all dimensionless wave lengths are satisfied with Figure 4.8.

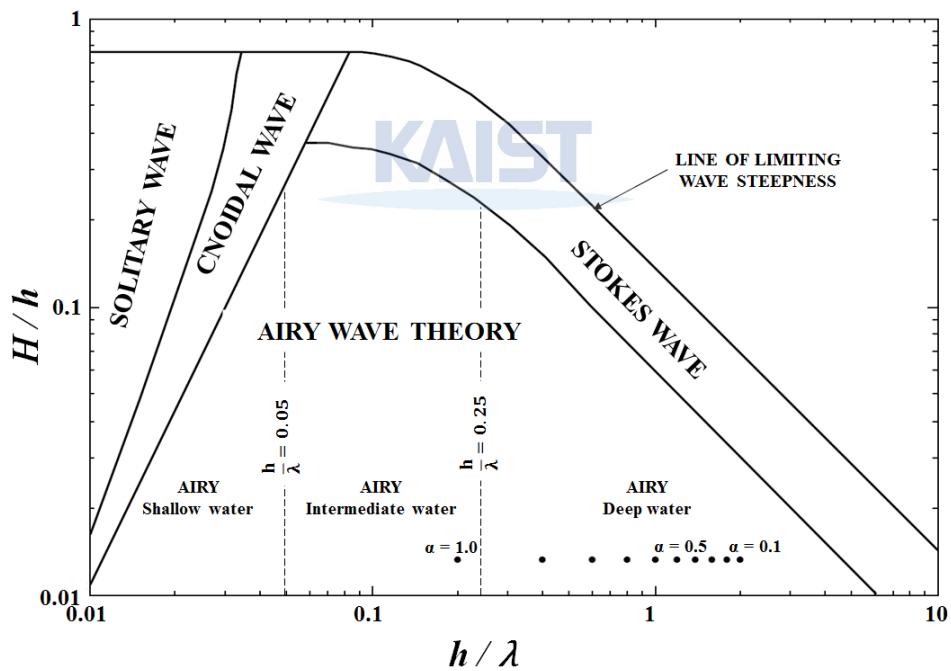
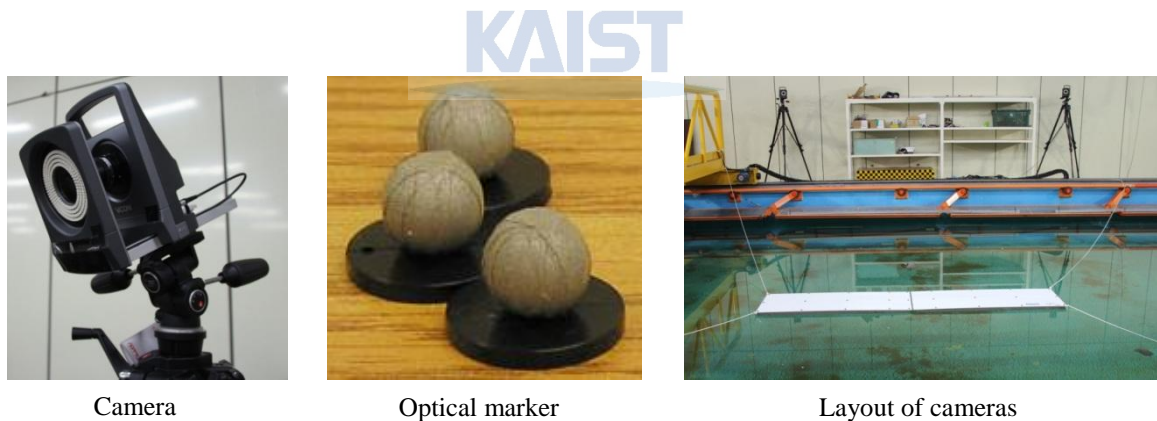


Figure 4.8: Ranges of validity of various wave theories as a function of  $H/h$  and  $h/\lambda$

## 4.5 Measuring methods

The equipment for tests consisted of three major elements: a motion capture system for heave motion, a strain gauge for bending moment, and a wave probe for wave frequency and amplitude. In every experiment, we needed to measure the incident wave amplitude. In order to measure the wave frequency and amplitude at the front side of the floating structure, one wave probe was installed at the front side, as illustrated in Figure 4.2. One wave probe was positioned at the free water surface, a distance of about 1 meter from the front part of the floating structure. The wave probes measured the wave elevation with respect to time at their locations.

In order to measure the heave motion, we employed a Vicon motion capture system with optical markers. The Vicon motion capture system consists of three parts: a motion camera, main system, and optical marker. Four cameras could measure the heave motion of the marker without missing data or a dead angle. Moreover, the resolution was one micrometer, thus providing very small error. A total of 24 markers were attached to each of the portside, center, and starboard on top of the floating structure with no hinge connection, and then 3 markers were added when one hinge connection was added. The positions of the markers are shown in Figure 4.10.



Model	MX T-20S
Type	Infrared
Resolution	2 megapixel, 690 FPS (1600×1280)
Accuracy	50μm

Specification of camera

Figure 4.9: Vicon motion capture system

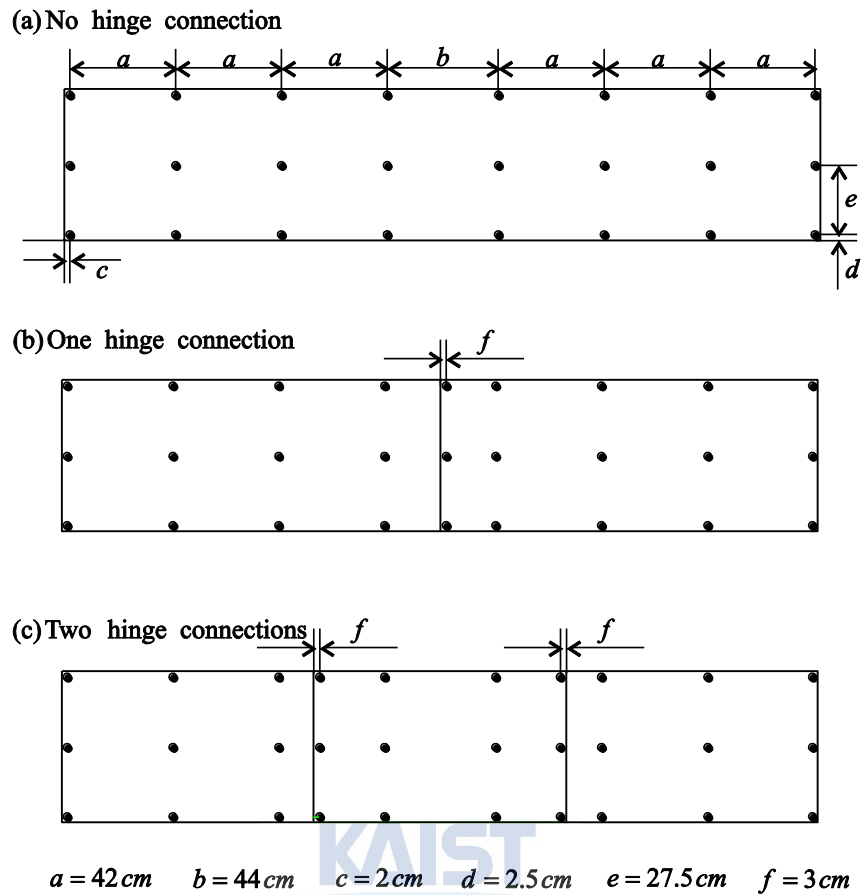


Figure 4.10: The measuring position of heave motion

For measuring strain, we utilized a strain gauge with a DAQ system. The strain gauge could measure the strain on the floating structure acting on the incident wave with various angles and frequencies. Three axial element strain rosettes were employed to measure the bending moment in the direction of  $0^\circ$ ,  $45^\circ$ , and  $90^\circ$  on the deck points. Therefore, we measured three kinds of strain:  $\varepsilon_{11}$ ,  $\varepsilon_{22}$ , and  $\gamma_{12}$ . The positions of the strain gauges are shown in Figure 4.12.

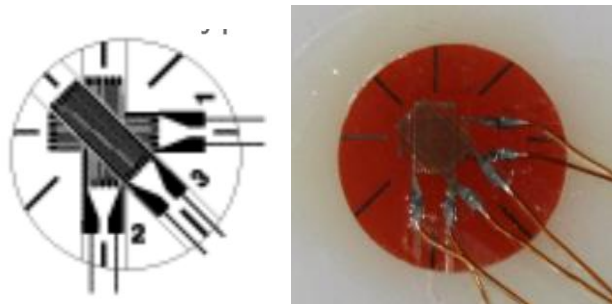
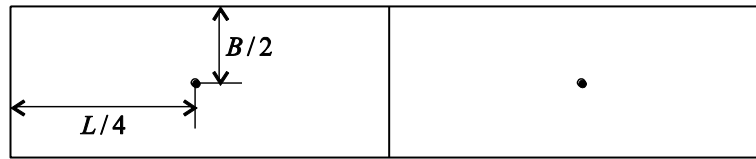


Figure 4.11: Three elements strain rosette

(a) One hinge connection



(b) Two hinge connections

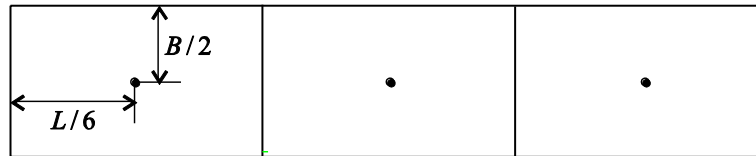


Figure 4.12: The measuring position of strain gauge

KAIST

## Chapter 5. Results

In this chapter, we compare the experimental results and conduct a numerical analysis of the heave motion and bending moment. The hydroelastic behavior of a floating structure depends on properties, such as bending stiffness, aspect ratio, wave frequency, and amplitude. The floating structure was fixed by the bending stiffness and the aspect ratio. The floating structure without a hinge connection was tested first, then we conducted experiment with the hinge connected floating structure via same procedure.

### 5.1 Heave motion

Hydroelastic behaviors have a variety of motions such as surge, sway, heave, roll, pitch, and yaw. Among those, heave motion is the most important for floating structures in the ocean environment. Therefore, we measured heave motion at the portside, center, and starboard of the floating structure. From Figures 5.2 to 5.13, we provide a comparison of the experimental results and numerical analysis of the heave motion's response amplitude operator (RAO) value, that is, the heave motion divided by incident wave amplitude ( $u_3/A$ ) at  $\alpha = 0.1 \sim 1.0$  and  $0 \sim 90^\circ$ . The X axis is the position divided by the structural length ( $x/L$ ). The figures are consistent with the overall trend of the experimental and numerical results. Therefore, the experimental results are in accordance with the numerical analysis results.

By adding a hinge connection to the floating structures, heave motion is slightly increased. In order to decrease heave motion, the floating structure should be equipped with an anti-heaving device that is proved to effectively decrease heave motion. K. Takagi [18] investigated the effectiveness of an anti-heaving device composed of a box-shaped body attached to an edge of a VLFS with a theoretical method and experiments.

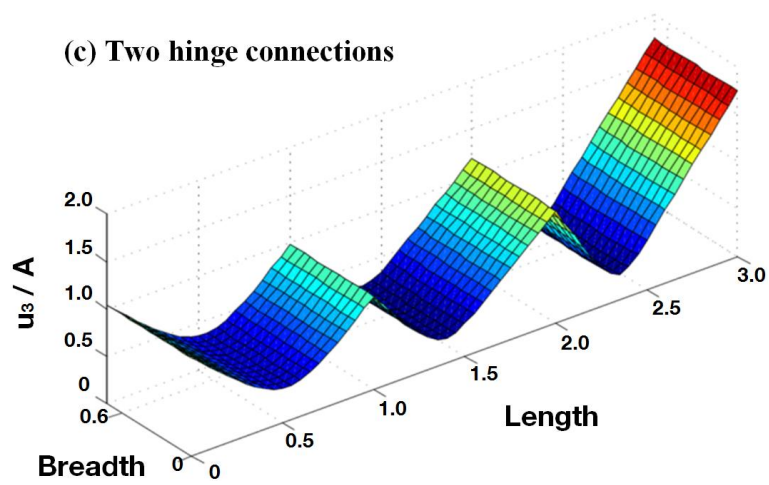
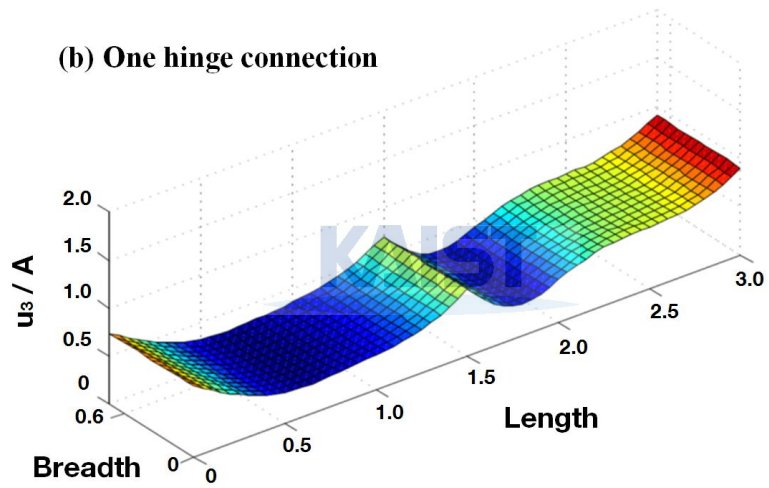
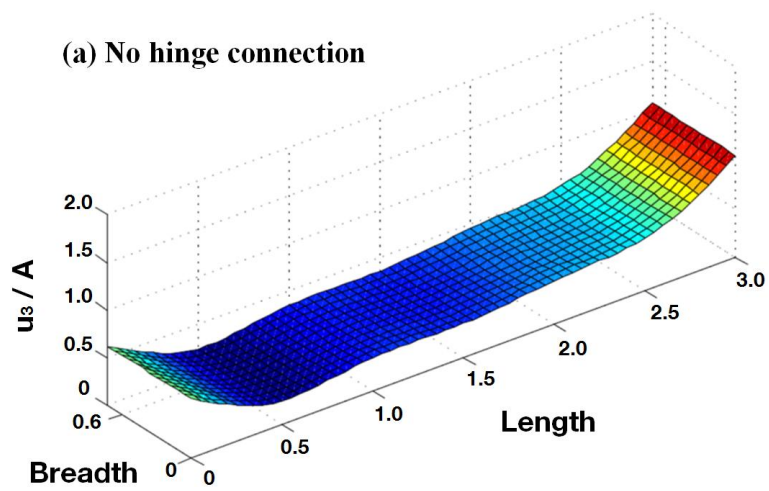


Figure 5.1: Distribution of heave motion at  $\alpha = 0.6$

$$\theta = 0^\circ$$

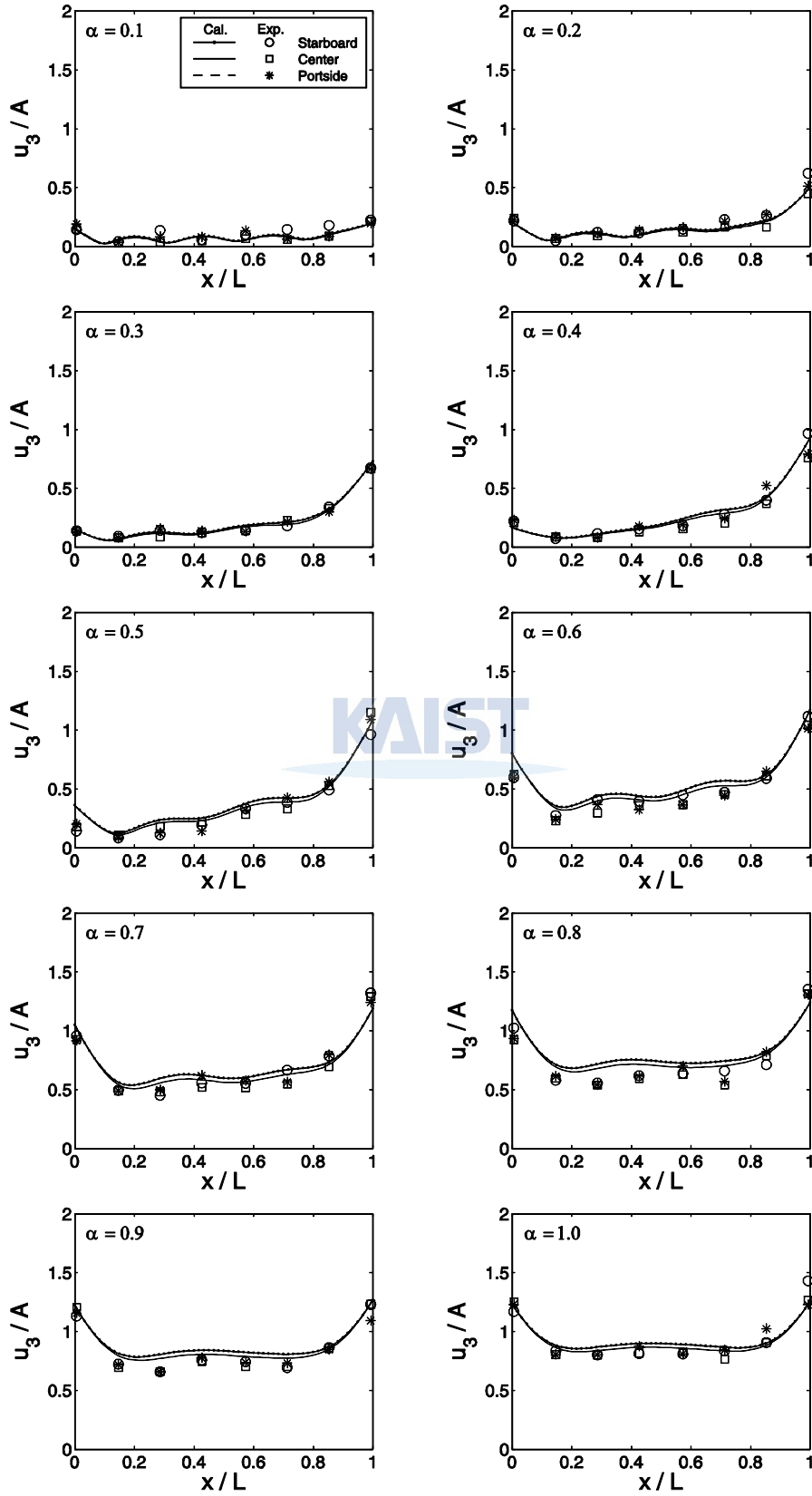


Figure 5.2: Longitudinal distributions of heave motion (No hinge connection at  $\theta = 0^\circ$  )

$\theta = 30^\circ$

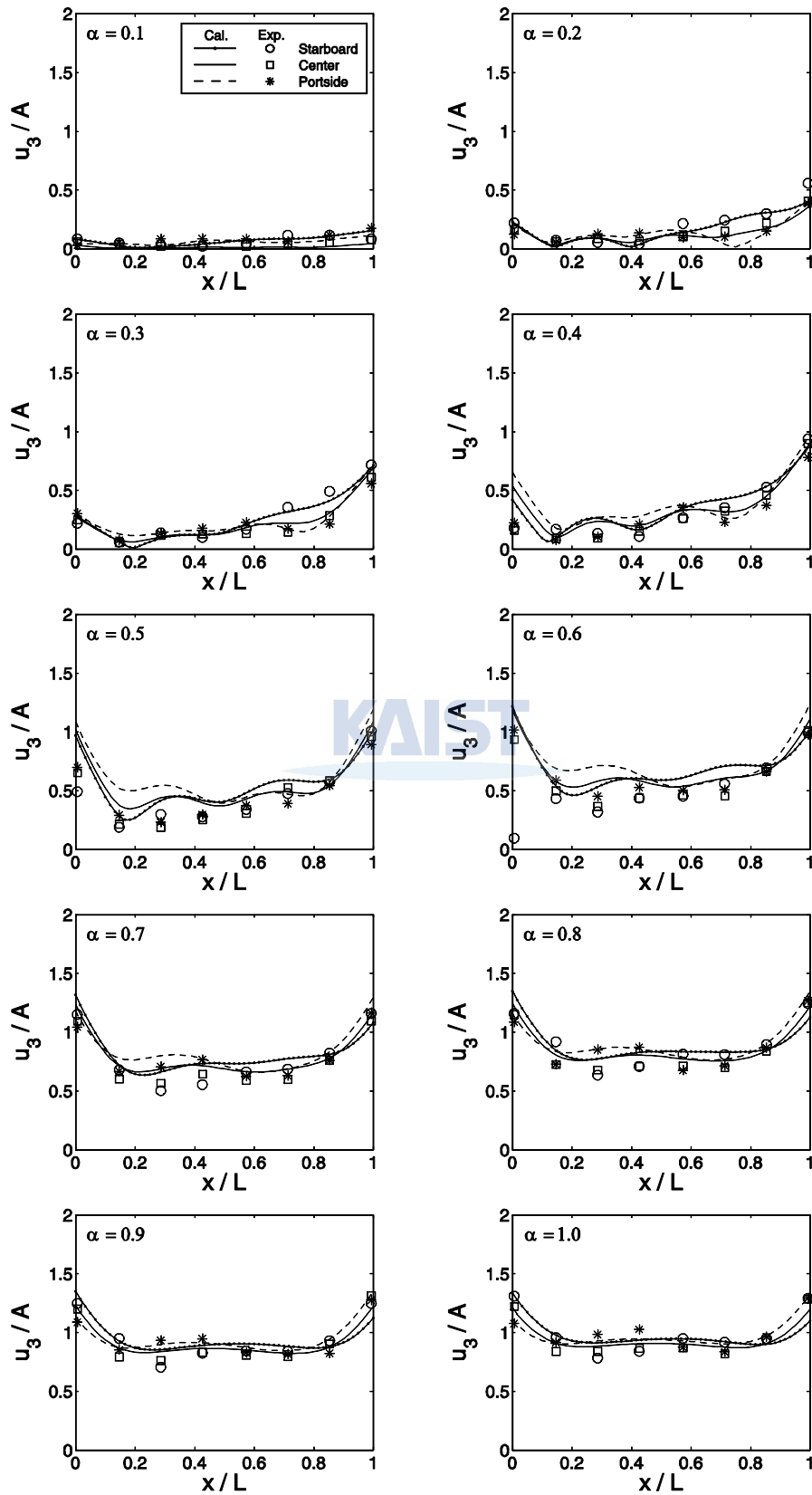


Figure 5.3: Longitudinal distributions of heave motion (No hinge connection at  $\theta = 30^\circ$  )

$\theta = 60^\circ$

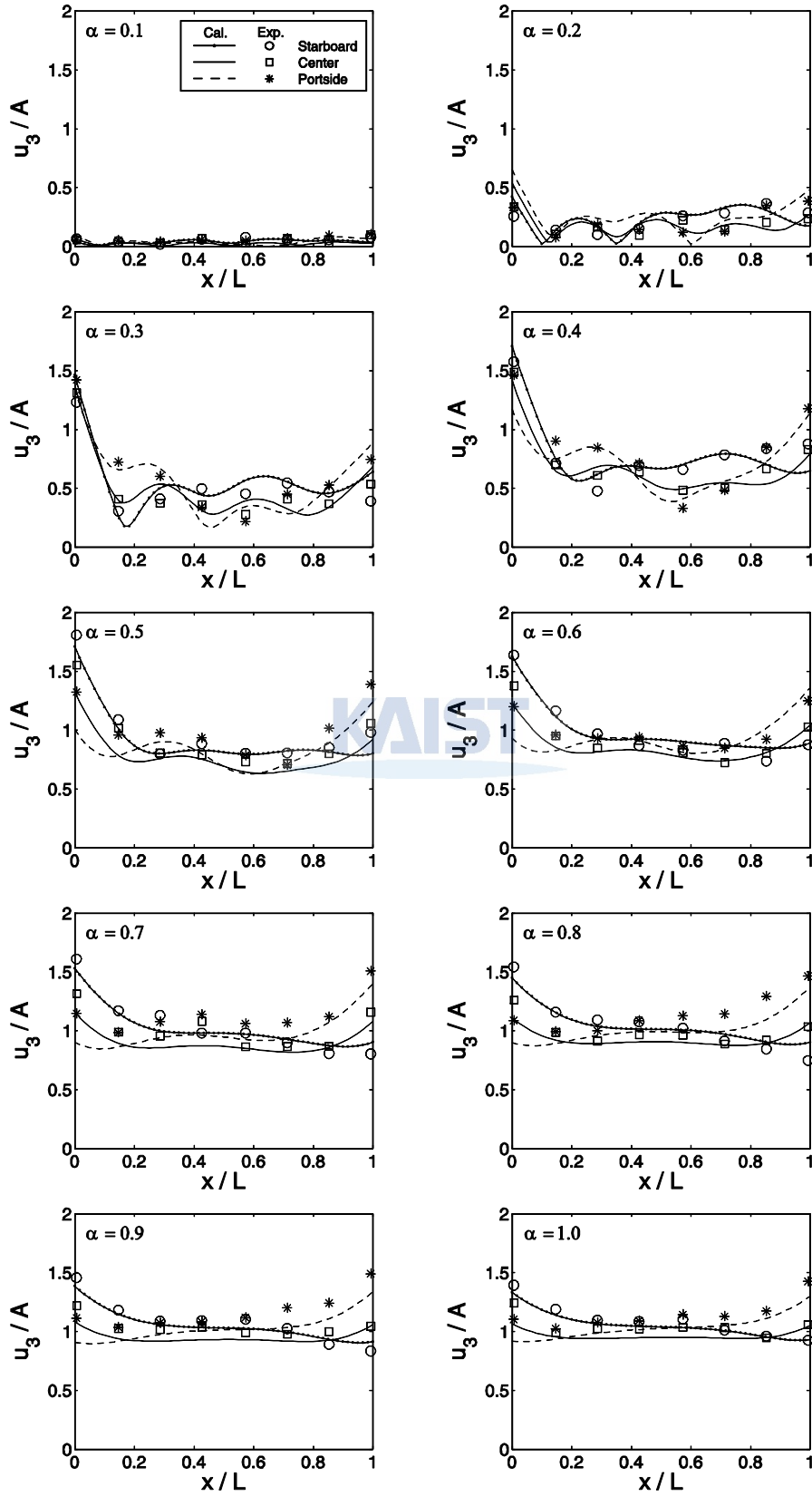


Figure 5.4: Longitudinal distributions of heave motion (No hinge connection at  $\theta = 60^\circ$  )

$\theta = 90^\circ$

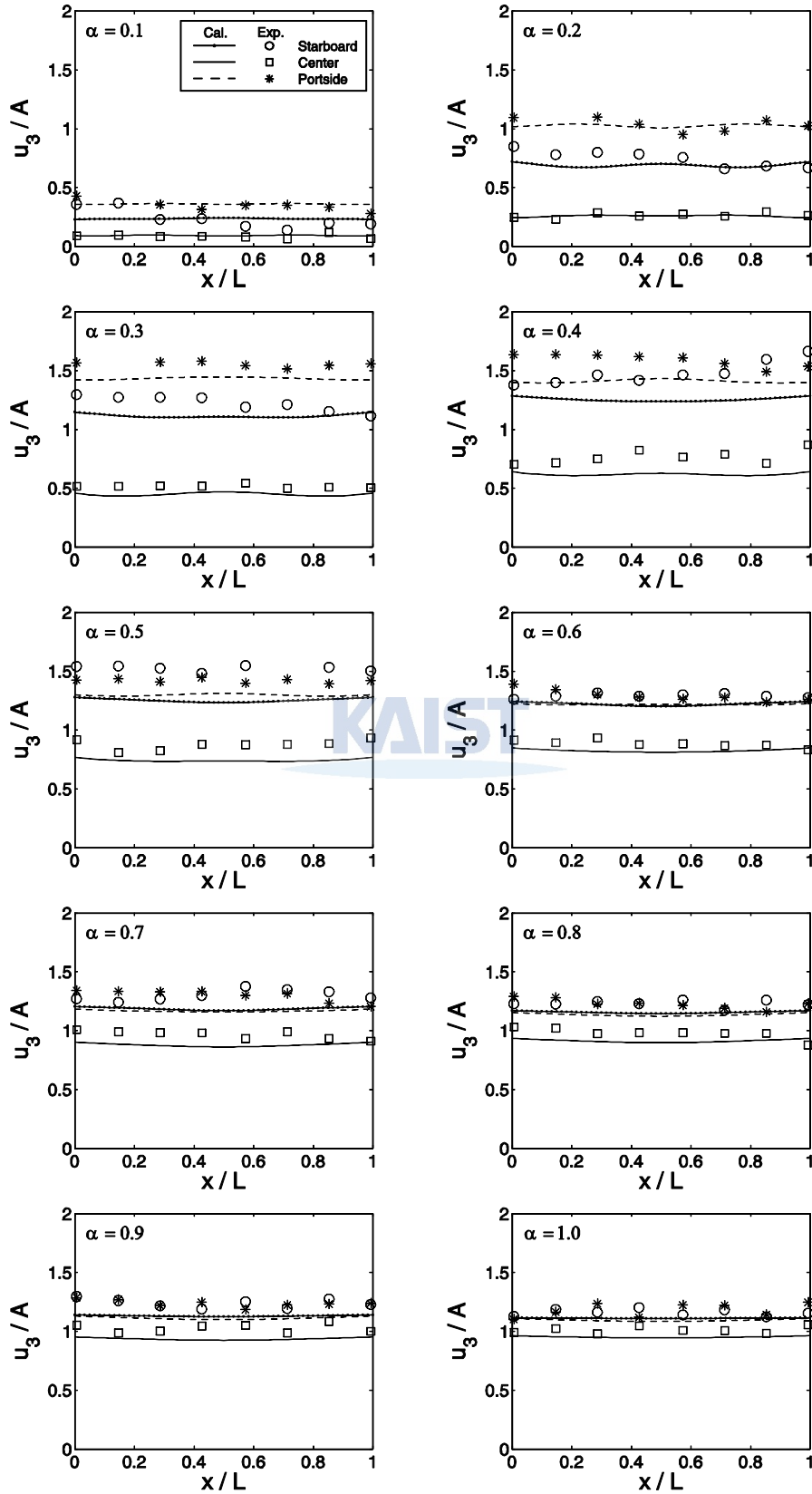


Figure 5.5: Longitudinal distributions of heave motion (No hinge connection at  $\theta = 90^\circ$  )

$\theta = 0^\circ$

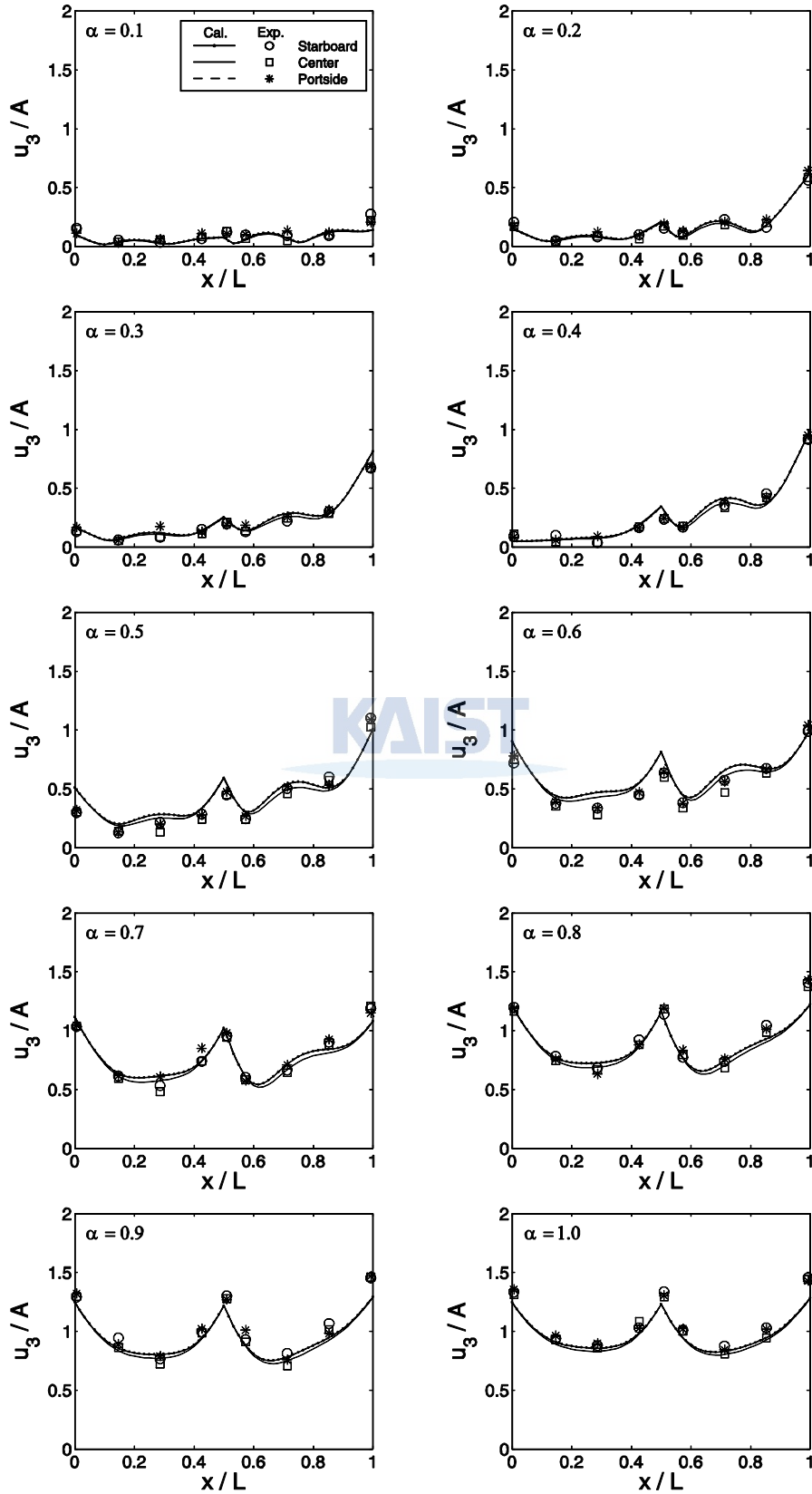


Figure 5.6: Longitudinal distributions of heave motion (One hinge connection at  $\theta = 0^\circ$  )

$\theta = 30^\circ$

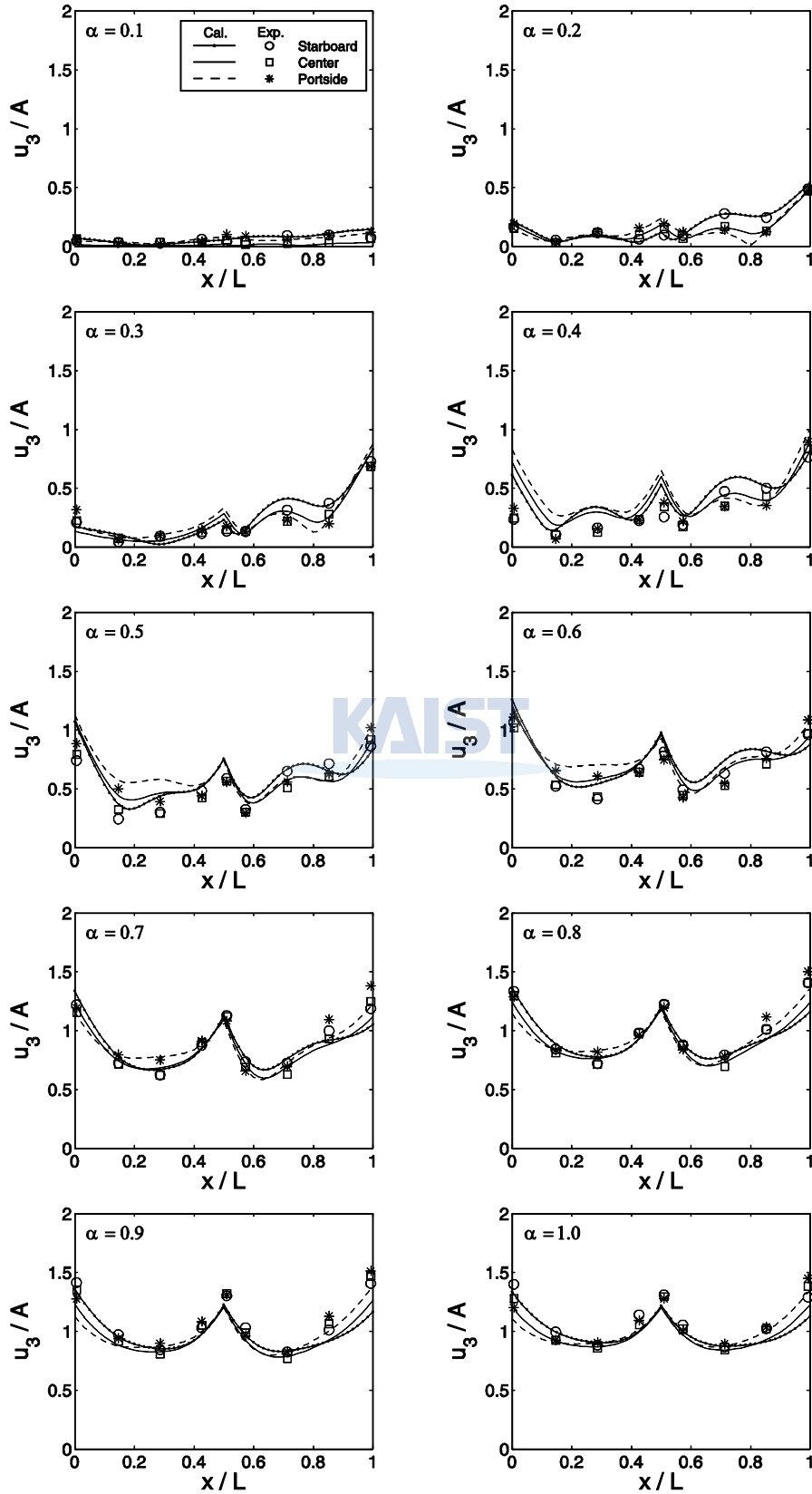


Figure 5.7: Longitudinal distributions of heave motion (One hinge connection at  $\theta = 30^\circ$  )

$\theta = 60^\circ$

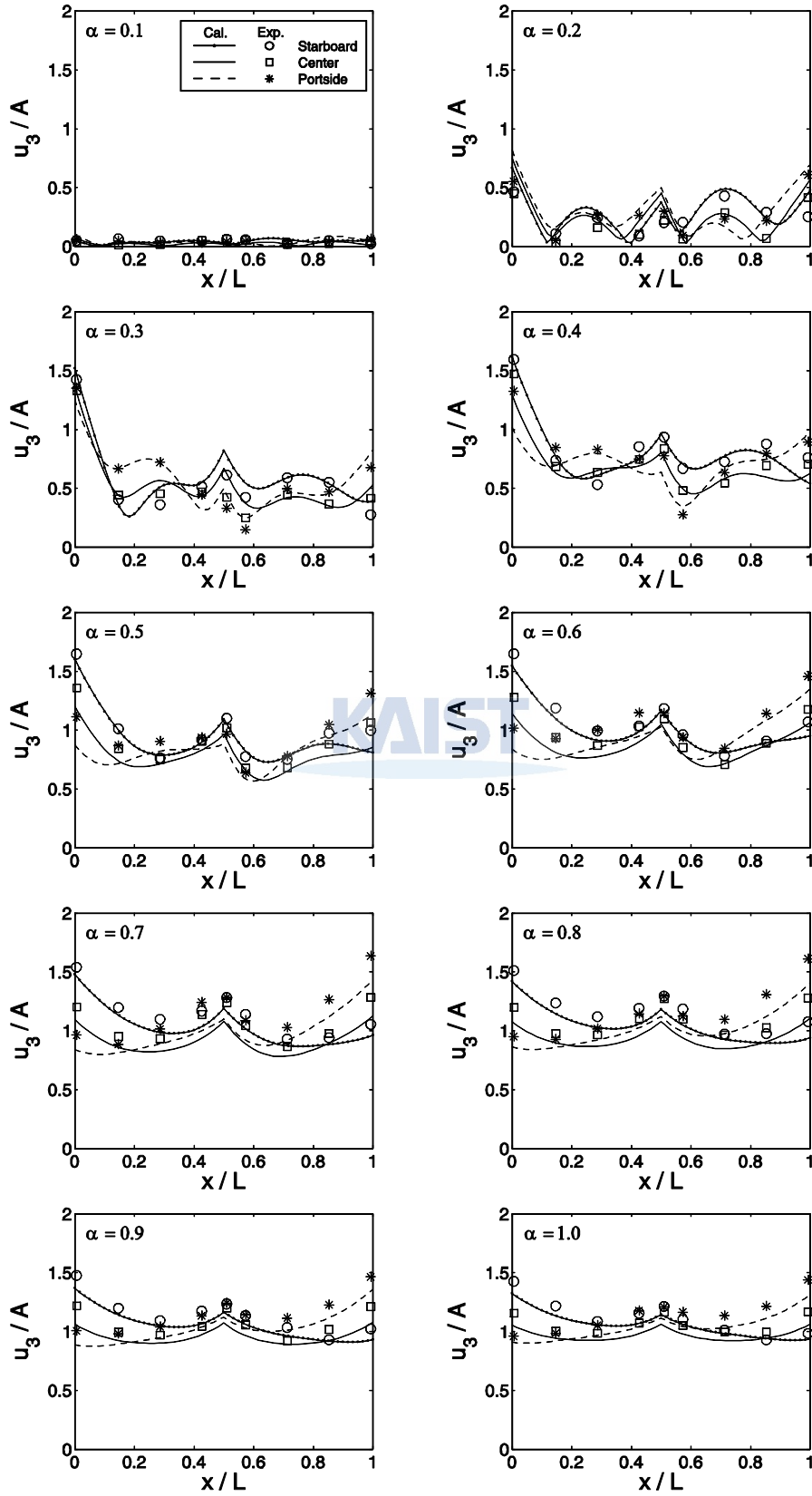


Figure 5.8: Longitudinal distributions of heave motion (One hinge connection at  $\theta = 60^\circ$  )

$\theta = 90^\circ$

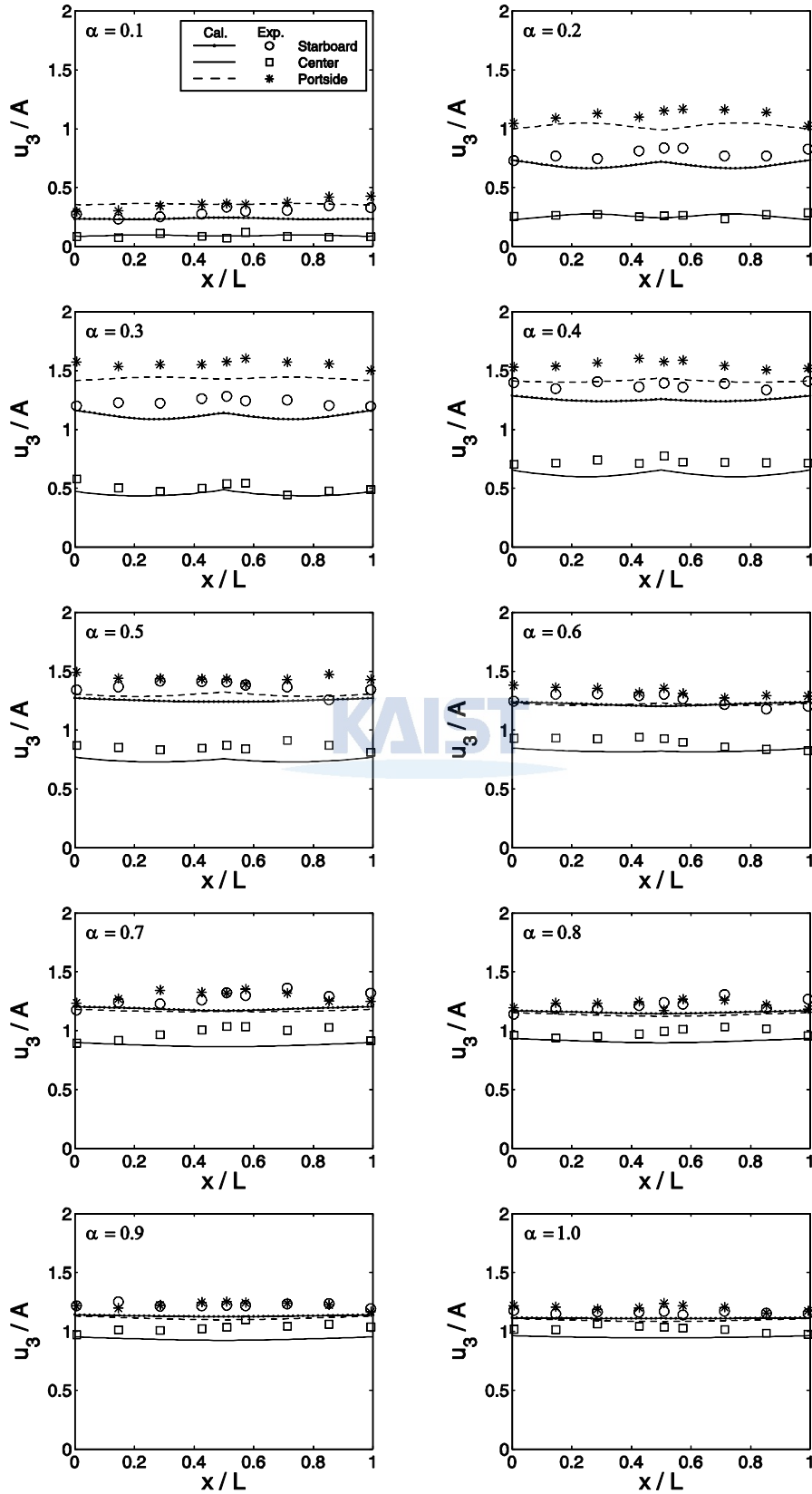


Figure 5.9: Longitudinal distributions of heave motion (One hinge connection at  $\theta = 90^\circ$  )

$$\theta = 0^\circ$$

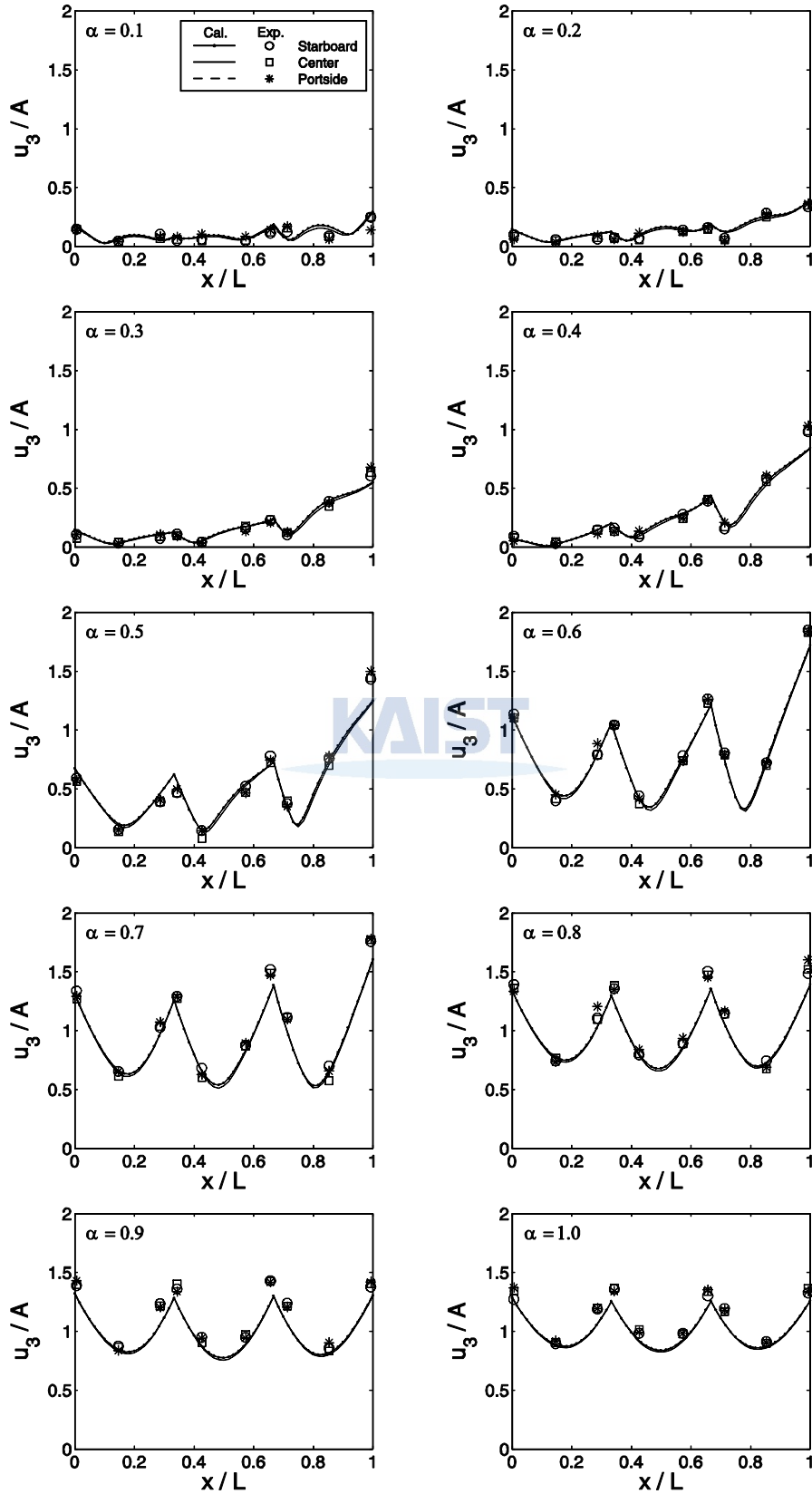


Figure 5.10: Longitudinal distributions of heave motion (Two hinge connection at  $\theta = 0^\circ$  )

$\theta = 30^\circ$

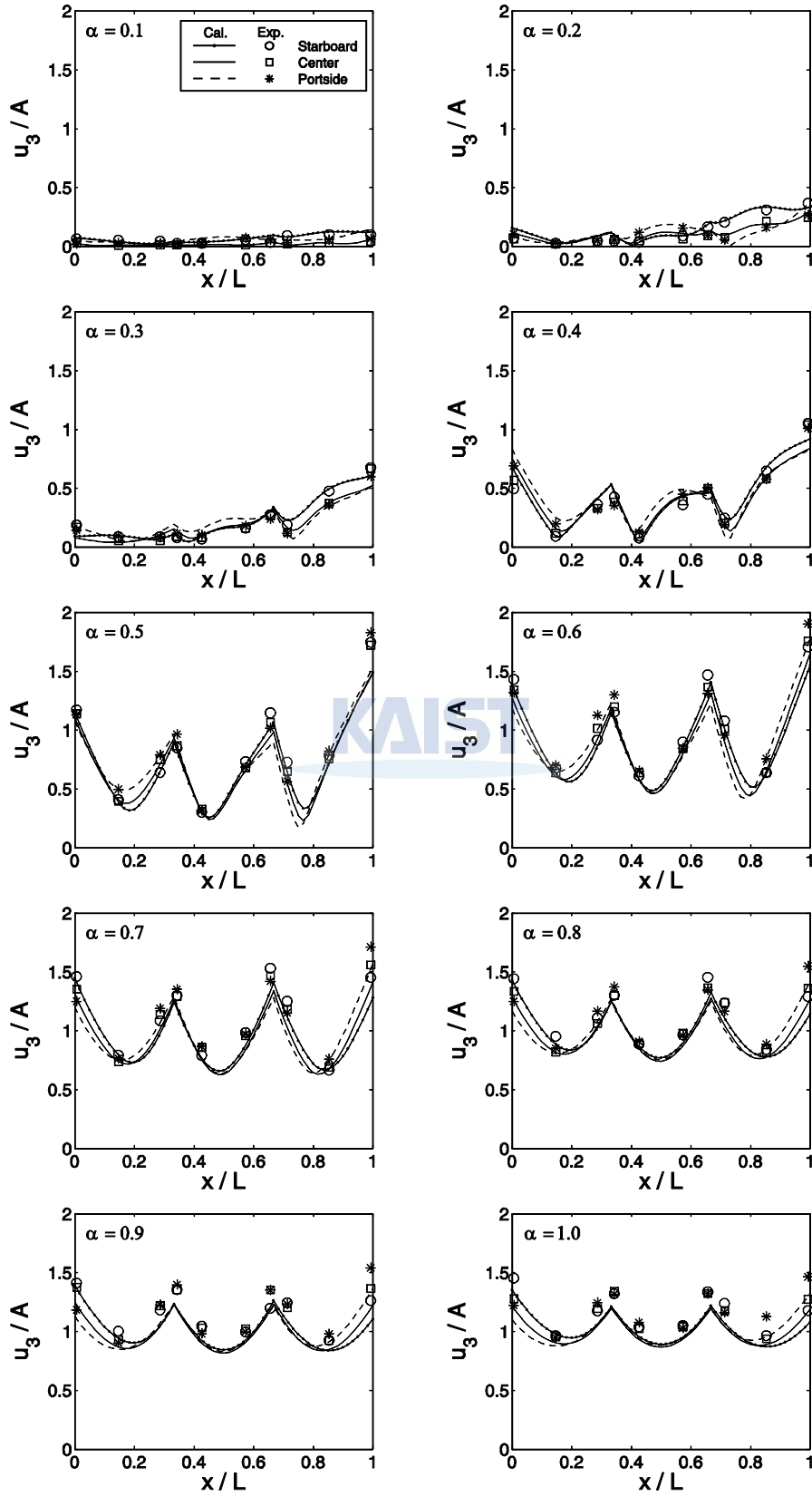


Figure 5.11: Longitudinal distributions of heave motion (Two hinge connection at  $\theta = 30^\circ$  )

$\theta = 60^\circ$

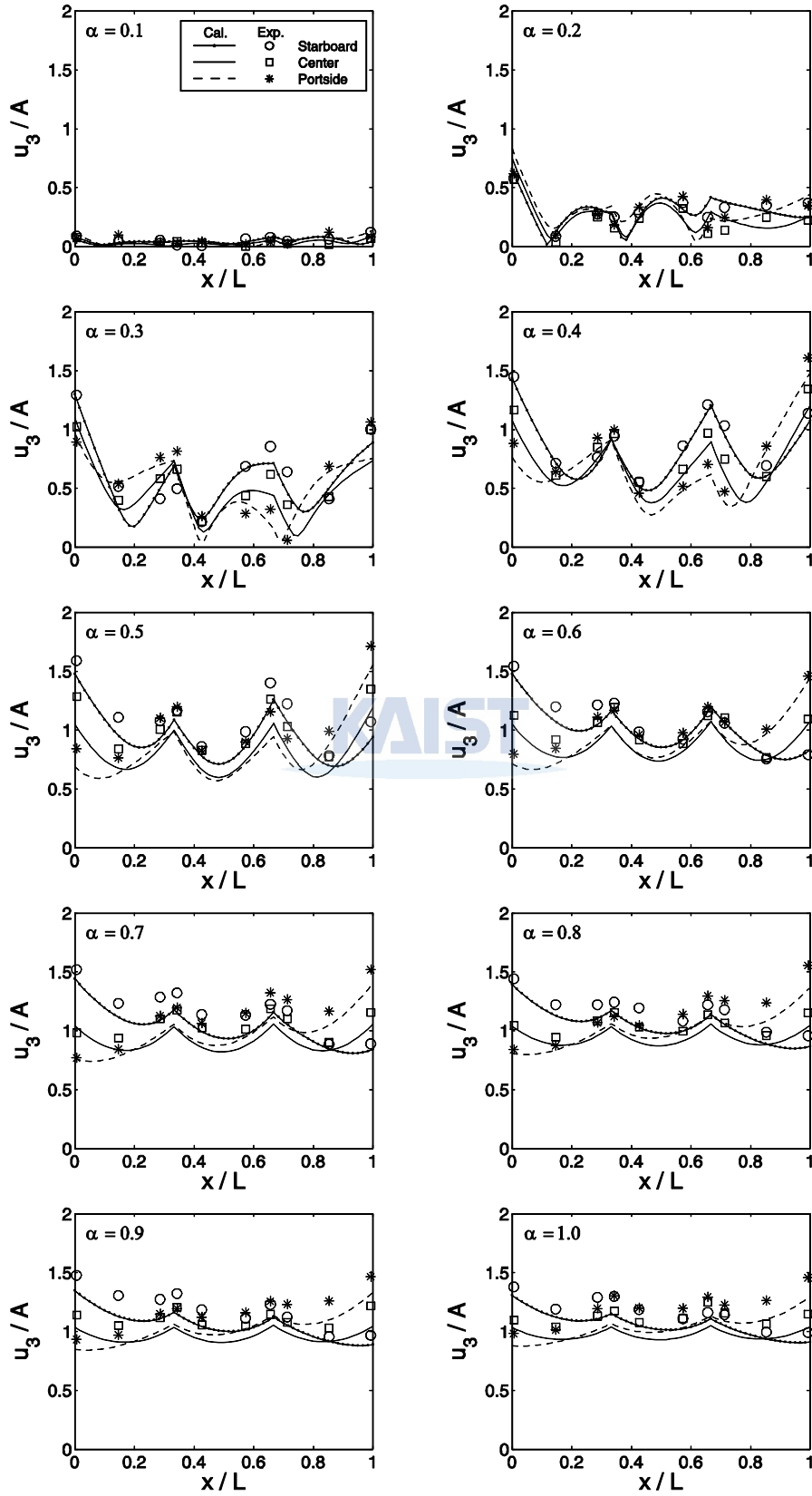


Figure 5.12: Longitudinal distributions of heave motion (Two hinge connection at  $\theta = 60^\circ$  )

$\theta = 90^\circ$

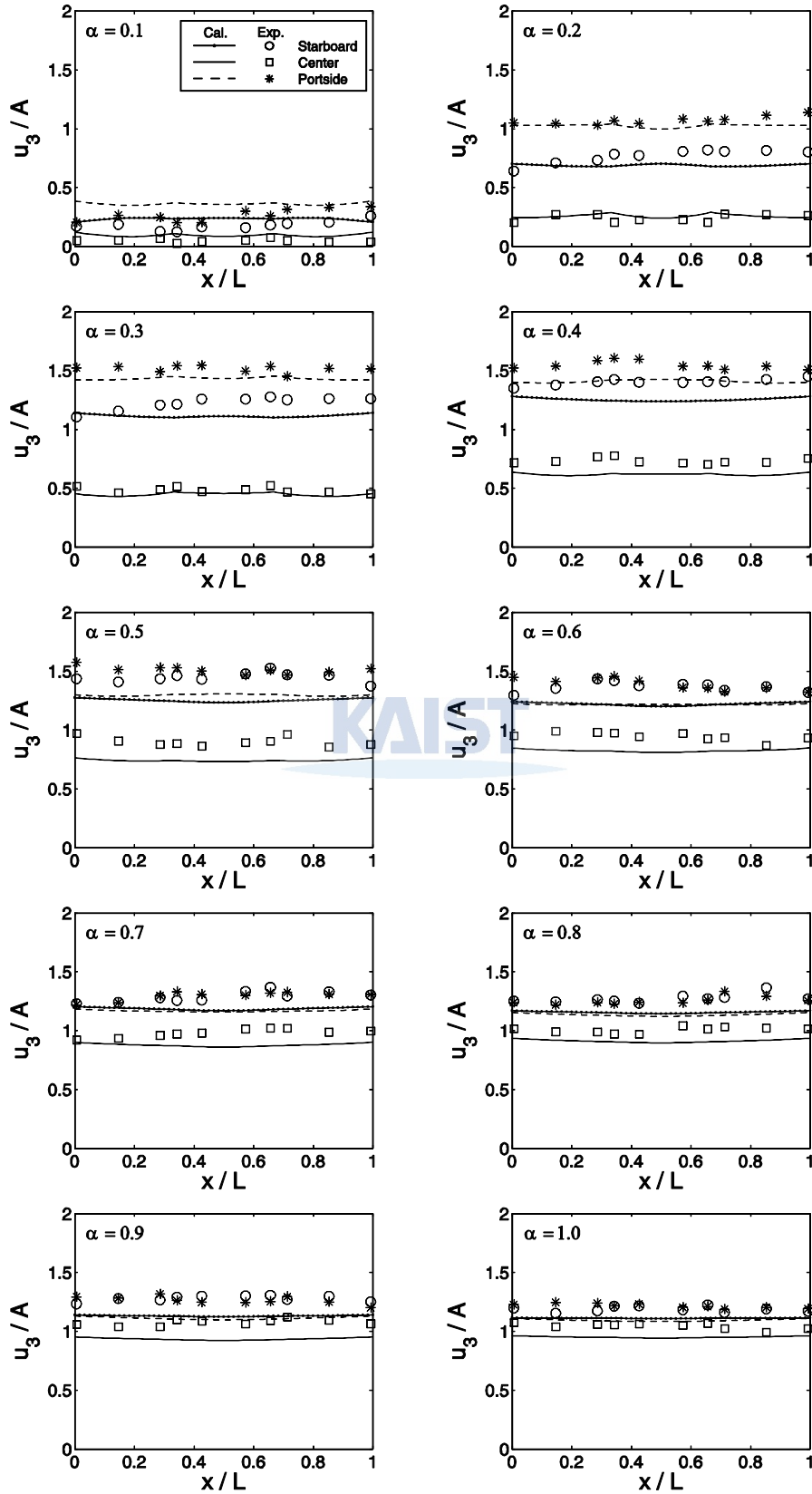


Figure 5.13: Longitudinal distributions of heave motion (Two hinge connection at  $\theta = 90^\circ$  )

## 5.2 Bending moment

The main problem is reducing bending moment in the floating structure, since it is related to the life of the structure. We utilized strain gauges for measuring the bending moment. Eq. (5.1) illustrates the relationship between strain and bending moment. Three axial element strain rosettes were employed to measure the bending moment in the directions of 0, 45, and 90° on the deck points. Hence, we measured three kinds of strain,  $\varepsilon_{11}$ ,  $\varepsilon_{22}$ , and  $\gamma_{12}$ . Also, curvature values  $\kappa_{ij}$  can be calculated by the strain values  $\varepsilon_{ij}$ .

$$\begin{bmatrix} M_{11} \\ M_{22} \\ M_{12} \end{bmatrix} = \frac{Et^3}{12(1-\nu^2)} \begin{bmatrix} 1 & \nu & 0 \\ \nu & 1 & 0 \\ 0 & 0 & \frac{1}{2(1+\nu)} \end{bmatrix} \begin{bmatrix} \kappa_{11} \\ \kappa_{22} \\ 2\kappa_{12} \end{bmatrix}, \quad \kappa_{ij} = \frac{\varepsilon_{ij}}{x_3} \quad (5.1)$$

In the numerical analysis, we assumed a neutral axis was positioned at the middle of the section, which corresponds with  $t/2$ . However, the neutral axis was positioned at the middle of the polycarbonate plate with the actual physical phenomenon of bending behavior, because polyethylene foam has much smaller bending stiffness than the polycarbonate plate. Therefore, we calculated the curvatures  $\kappa_{11}$ ,  $\kappa_{22}$  as measured strain values and calculated the length of  $x_3$ . Figure 5.14 illustrates the position of the actual neutral axis.  $x_{3-N}$  denotes the length from the bottom to the neutral axis.

Figures 5.16 to 5.19 present a comparison of the experimental results and numerical analysis of the bending moment's response amplitude operator (RAO) value in  $M_{11}$  at  $\alpha = 0.2 \sim 1.0$  and  $0 \sim 90^\circ$ .

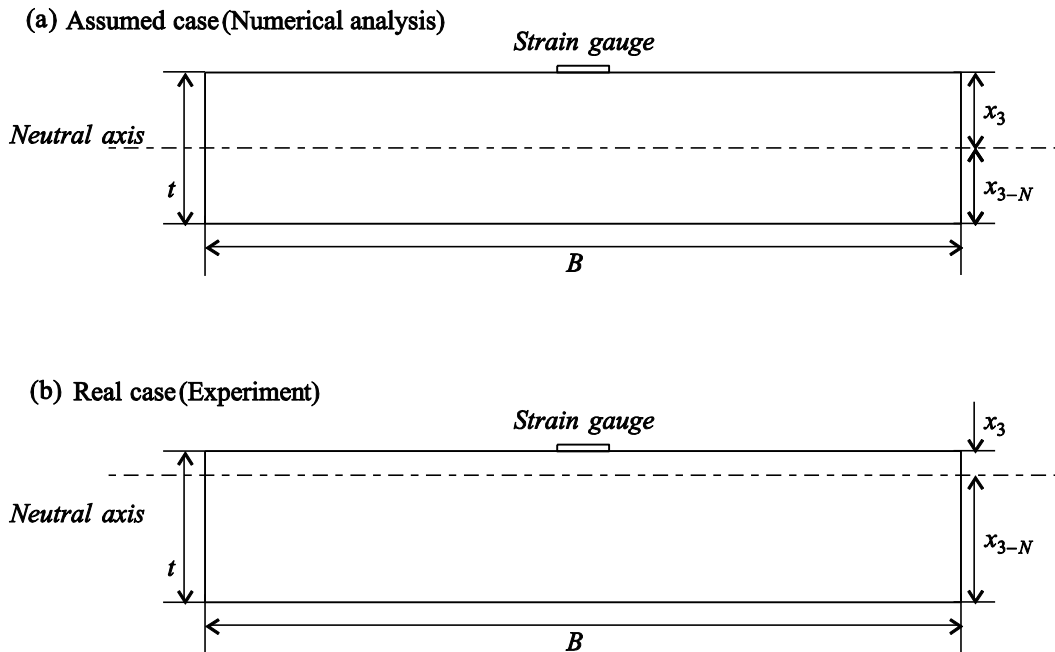


Figure 5.14: The position of neutral axis

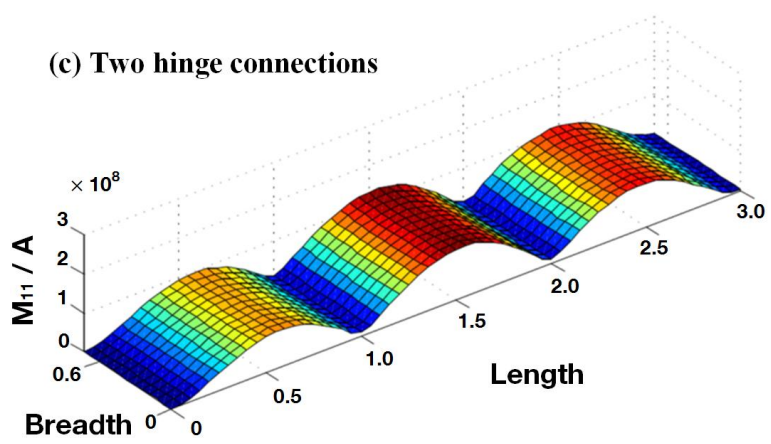
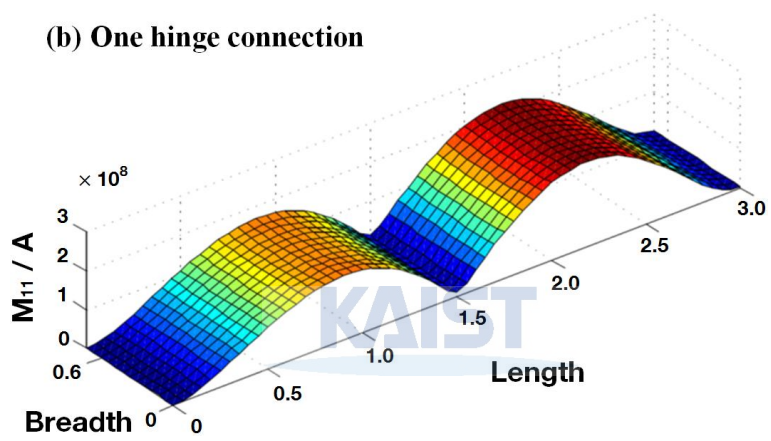
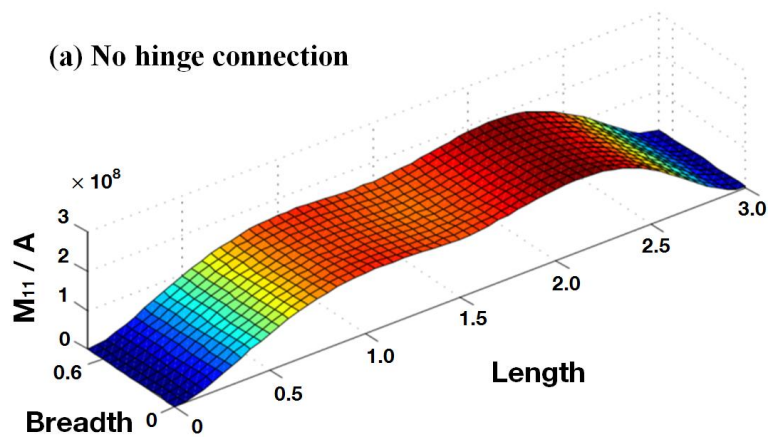


Figure 5.15: Distribution of bending moment at  $\alpha = 0.6$

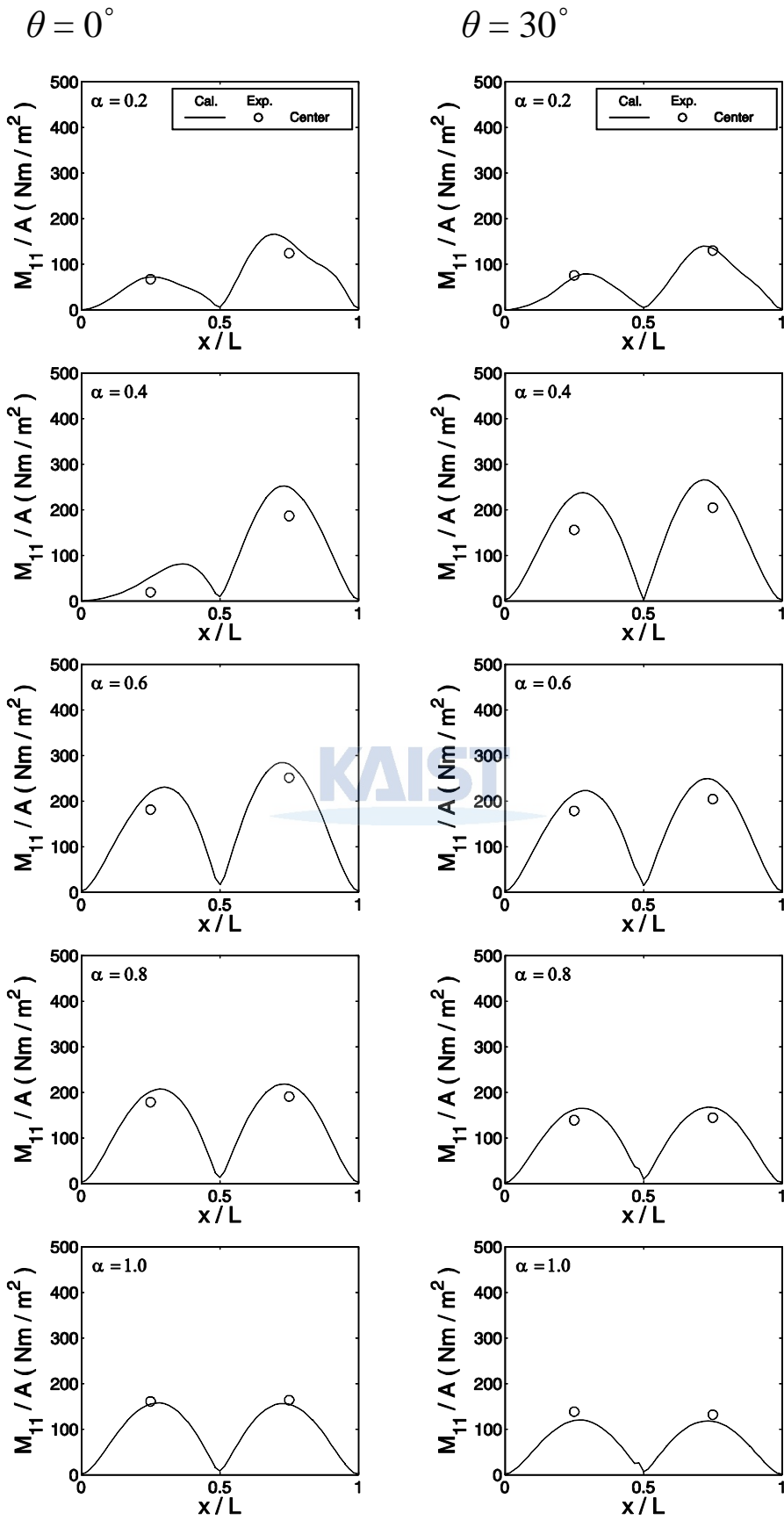


Figure 5.16: Longitudinal distributions of bending moment (One hinge connection at  $\theta = 0, 30^\circ$  )

$\theta = 60^\circ$

$\theta = 90^\circ$

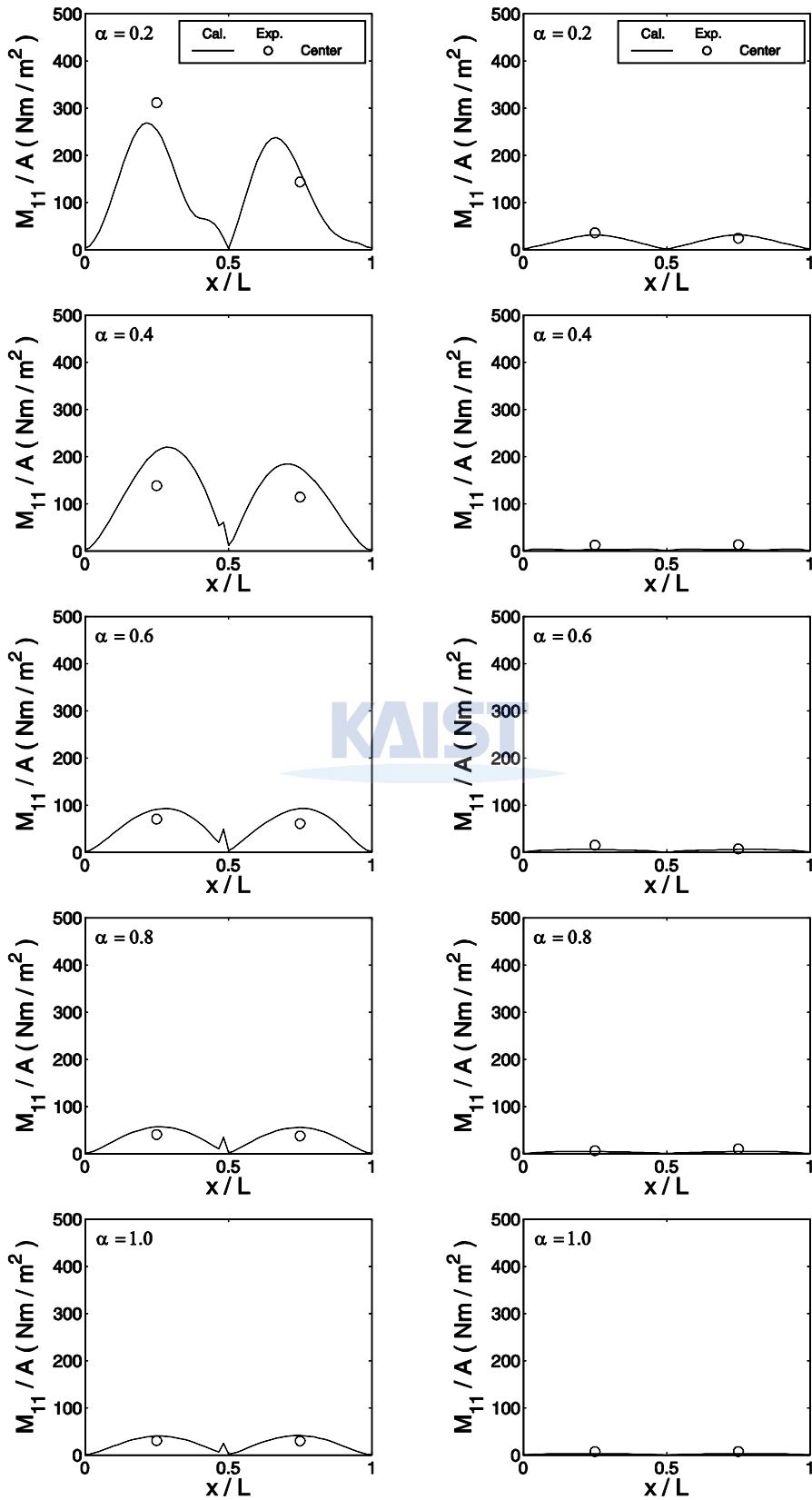


Figure 5.17: Longitudinal distributions of bending moment (One hinge connection at  $\theta = 60, 90^\circ$  )

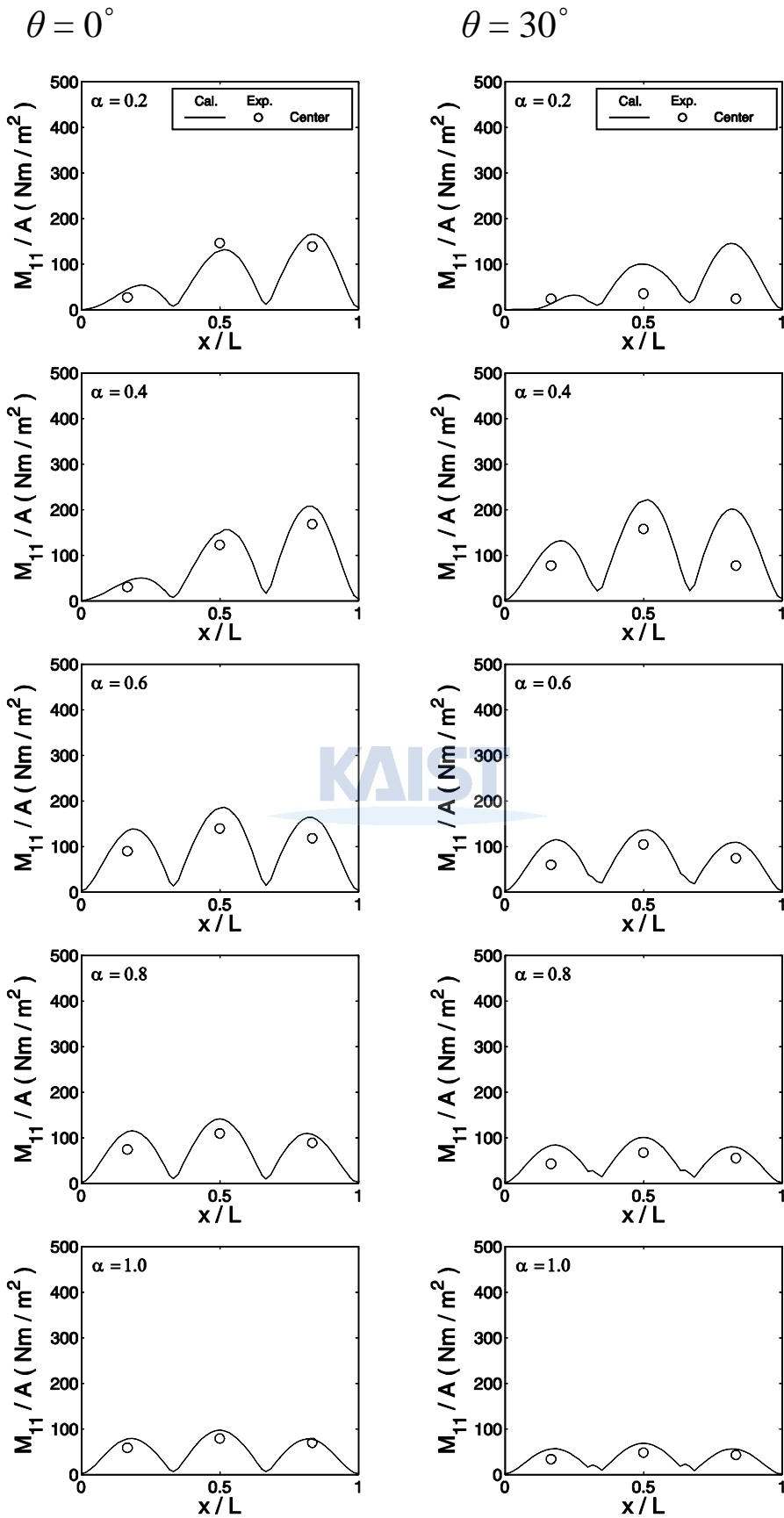


Figure 5.18: Longitudinal distributions of bending moment (Two hinge connection at  $\theta = 0, 30^\circ$  )

$\theta = 60^\circ$

$\theta = 90^\circ$

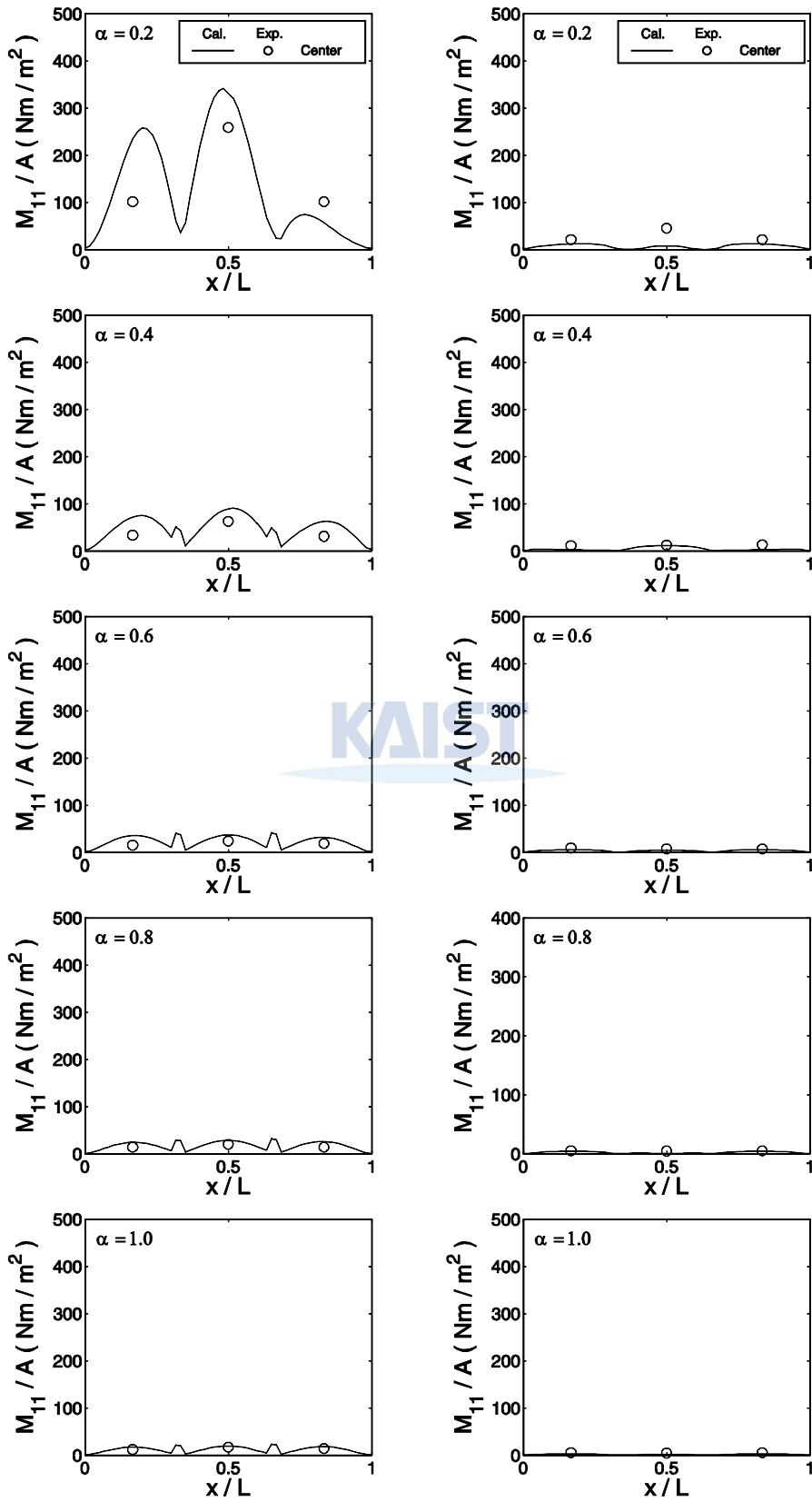


Figure 5.19: Longitudinal distributions of bending moment (Two hinge connection at  $\theta = 60, 90^\circ$  )

## Chapter 6. Conclusion

We have investigated the hydroelastic behavior of a floating structure under regular waves in the frequency domain with numerical and experimental studies. In the real world, it is necessary to consider the connection type used with floating structures due to the severe ocean environment. The hinge connection method is well known for reducing the bending moment acting on the cross section of these structures.

Numerical and experimental studies of the hydroelastic behavior of floating structures with hinge connections located at one side in regular waves was carried out in this study. The evaluation of hydroelastic behavior of floating structures focused on heave motion and bending moment. These behaviors depended on the incident wave frequency and angle. In the study of hydroelastic behavior, we described relevant mathematical formulations and the numerical procedure that we employed. With appropriate assumptions, we derived coupled equations in terms of the structural and fluid components for the hydroelastic analysis. In order to solve these equations, we employed the finite element method for the structural part and the boundary element method for the fluid part.

For validation of the numerical procedure, the floating structures were tested with three other proposed types, no hinge, one hinge connection, and two hinge connections. The numerical results were initially validated against the experimental results and subsequently used to conduct studies to investigate the effectiveness of hinge connections. Based on the results from the experiment and numerical analysis, the hinge connections reduced the bending moment of the floating structure. We expect that these experimental results may help to evaluate numerical analyses in relate research. Also, these results can be utilized in the design of revolutionary very large floating structures in the future.

## References

- [1] Yago, K. and Endo, H. (1997), "On the hydroelastic response of box-shaped floating structure with shallow draft", *Journal of the Society of Naval Architects of Japan*, Vol. 182, pp. 307-317.
- [2] Bathe, K. J. (1996), *Finite element procedures*, Prentice Hall, 1037 pages.
- [3] ISSC, Report of Special Committee VI.2 (2006), "Very Large Floating Structures," *Proceeding 16th International Ship and Offshore Structure Congress*, Vol 2, pp. 391-442.
- [4] Taylor, R. E. (2007). "Hydroelastic analysis of plates and some approximations, *Journal of Engineering Mathematics*, Vol. 58, pp. 267-278.
- [5] Kim, B. W., Hong, S. Y., Kyung, J. H. and Cho, S. K. (2006), "Dynamic response characteristics of floating structures according to connection types", *Journal of the Korea Society for Noise and Vibration Engineering*, Vol 16, pp. 132-140.
- [6] Khabakhpasheva, T.I. and Korobkin, A.A. (2002), "Hydroelastic behaviour of compound floating plate in waves", *Journal of engineering mathematics*, Vol. 44, pp. 21-40.
- [7] Kim, K. T. (2011). "Hydroelastic analysis of three-dimensional floating structures", *Master's Thesis*, Korea Advanced Institute of Science and Technology, Daejeon, Republic of Korea, 62 pages.
- [8] Wehausen, J.V. and Laitone, E.V. E. V. (1960), "Surface waves", *Encyclopedia of Physics*, Vol. 9, pp. 446-778.
- [9] Newman, J. N. (1985), "Algorithms for the free-surface Green function", *Journal of Engineering Mathematics*, Vol. 19, pp. 57-67.
- [10] WAMIT (2011), *User Manual Version 7.0*, WAMIT Inc.
- [11] Lee, C. H. and Newman, J. N. (2000), An assessment of hydroelasticity for very large hinged vessels, *Journal of Fluids and Structures*, Vol. 14, pp. 957-970.
- [12] Journ e, J.M.J. and Massie, W. W. (2001), *Offshore Hydrodynamics*, Delft University of Technology, 650pages.

- [13] Wang, C. M., Watanabe, E. and Utsunomiya, T. (2008), *Very Large Floating Structures*, Taylor & Francis, London and New York, 235 pages.
- [14] Timoshenko, S.P., Krieger W. (1970), *Theory of plates and shells 2/e*. McGraw-Hill, 580 pages.
- [15] Dean, R. G. and Dalrymple, R. A. (1984). *Water Wave Mechanics for Engineers and Scientist*, Prentice Hall, 353 pages.
- [16] Fu, S., Moan, T., Chen, X. and Cu, W. (2007), “Hydroelastic analysis of flexible floating interconnected structures”, *Ocean Engineering*, Vol. 34, pp. 1516-1531.
- [17] Riyansyah, M. (2009), “Hydroelastic response of interconnected floating beams modeling longish VLFS”, *Ph.D. Thesis*, National University of Singapore, Singapore, 245 pages
- [18] Takagi, K., Shimada, K. and Ikebuchi, T. (2000), “An anti-motion device for a very large floating structure”. *Marine structures*, Vol. 13, pp. 421-436.
- [19] Wehausen, J.V. and Laitone, E.V. (1960), “Surface waves”, *Encyclopedia of Physics*, Vol. 9, pp. 446-778.
- [20] Newman, J. N. (1985), “Algorithms for the free-surface Green function”, *Journal of Engineering Mathematics*, Vol. 19, pp. 57-67.
- [21] Suzuki, H. and Yoshida, K. (1996), “Design flow and strategy for safety of very large floating structure”, *Proceedings of International Workshop on Very Large Floating Structures, VLFS'96*, pp. 21-27.
- [22] Komar, P. D. (1976). *Beach Processes and Sedimentation*, New Jersey: Prentice-Hall, Inc., 429 pages
- [23] Jiwinangun, R. G. (2012). “Hydroelastic analysis of floating plate structures with hinge connections”, *Master's Thesis*, Korea Advanced Institute of Science and Technology, Daejeon, Republic of Korea, 59 pages
- [24] Reissner, E. (1945). “The effect of transverse shear deformation on the bending of elastic plate”, *Journal of Applied Mechanics*, Vol. 67, pp. A69-77.
- [25] Mindlin, R. D. (1951), “Influence of rotary inertia and shear on flexural motion of isotropic elastic plates”, *Journal of Applied Mechanics*, Vol. 18, pp. 31-38.

## Summary

### 부유식 구조물의 유탄성 거동에 관한 수치적 및 실험적 연구

본 연구의 목적은 수치적 및 실험적 연구로써 주파수 영역 내의 규칙 표면파의 작용하에 부유식 평판 구조물의 유탄성 거동을 해석하는 것이다. 구조물의 유탄성 해석을 위하여 판 구조물로 모델링하여 거동을 살펴본다. 먼저 연구에 관한 수학적 모델을 제시 한 후 수치해석기법으로 구조물의 유탄성 거동, 즉 수직 변위와 굽힘 모멘트를 계산한다. 이러한 수치적 연구를 검증 하기 위해 평판 모델로써 3 차원 수조내에 수치적 연구와 동일한 조건으로 유탄성 실험을 수행한다. 실험 결과로써 다른 유탄성 관련 연구를 검증 할수 있는 하나의 기준을 제시한다.

핵심어: 부유식 구조물, 유한요소법, 경계요소법, 힌지연결, 수직변위, 굽힘모멘트

The logo for KAIST (Korea Advanced Institute of Science and Technology) is displayed in a light blue color. It consists of the letters 'KAIST' in a bold, sans-serif font, with a horizontal line underneath the letters.